Electronic Supplementary Information:

Do metastable polymorphs always grow faster? Measuring and comparing growth kinetics of three polymorphs of tolfenamic acid

Pietro Sacchi*, Petros Neoptolemou, Roger Davey, Susan Reutzel-Edens, Aurora Cruz-Cabeza*

Table of contents

1. Crystal growth kinetics of polymorphic systems

Table S1 reports a summary of polymorphic systems for which crystal growth kinetics in pure solvents have been measured previously. Although this list is most likely incomplete, it reflects the scarcity of available data regarding crystal growth kinetics of polymorphs.

The table reports the type of experimental measurement (single crystal vs. batch reactor), the dimensions that were measured during the experiments, a qualitative comparison of the polymorphs' growth rates and a comment indicating if concomitant polymorphism has been observed for the polymorphs in question. The conclusions about which polymorph grows faster are based on observations made by the original authors of each cited work. Because sometimes growth rates were compared in terms of relative driving force only (supersaturation), an additional comment was added if comparison of the original data against solution concentration results in a different conclusion.

Table S1. Polymorphic systems with kinetic data in literature.

Compound	**Crystal forms**	**Growth rate Experiments[a]**	**Dimension(s) measured in experiments**	**Conclusions from original work**	**Concomitant Polymorphs?**
Stearic acid[1,2]	C (metastable < 32 °C) B (stable < 32 °C)	SC	(110) facet	B faster	Yes, in hexane at high supersaturation
Cimetidine[3]	A (metastable) B (stable)	BR	Mass of crystals	A faster relative to supersaturation; B faster relative to concentration	-
L-histidine[4]	A (stable) B (metastable)	BR	Mass of crystals	B grows faster relative to supersaturation; same growth rates relative to concentration	Yes
o-aminobenzoic acid[5]	I (stable) II (metastable)	SC	Diagonal of area-equivalent square	II faster at high supersaturation (S > 1.3); I faster at low S.	Yes
p-aminobenzoic acid[6]	α (stable) β (metastable)	SC	Length, Width	β significantly slower than α	-
Gestodene[7]	I (metastable < 18.5 °C) II (stable < 18.5 °C)	SC	Diagonal of area-equivalent square	Variable depending on supersaturation and temperature	Yes
Piracetam[8,9]	II (metastable) III (stable)	SC BR	Length, Width (SC) FBRM chord length (BR)	II faster relative to supersaturation; *III faster relative to concentration	Reported in n-propanol[10]
Aripiprazole[11]	III (metastable) V (stable)	SC	Length, Width	Similar growth rates relative to supersaturation; *V faster relative to solution concentration	Yes
[a]SC = Single Crystal, BR = Batch Reactor, *Not reported in original work, estimated in this work from original data					

2. Crystal structures of TFA-I, TFA-II and TFA-IX

All three polymorphs of TFA considered in this work crystallise in monoclinic crystal lattices with parameters as shown in Table S2 and their crystal packings are shown in Figure S1

Table S2. Crystallographic parameters of TFA-I, TFA-II and TFA-IX

Form	**CSD refcode**	**Space group**	**Z**	***a* (Å)**	***b* (Å)**	***c* (Å)**	**β (°)**
TFA-I	KAXXAI01	$P2_1/c$	4	4.826(2)	32.128(11)	8.041(4)	104.88(3)
TFA-II	KAXXAI	$P2_1/n$	4	3.836(2)	21.997(5)	14.205(7)	94.11(4)
TFA-IX	KAXXAI11	$P2_1/c$	4	10.5841(11)	7.8503(6)	14.9718(13)	101.399(9)

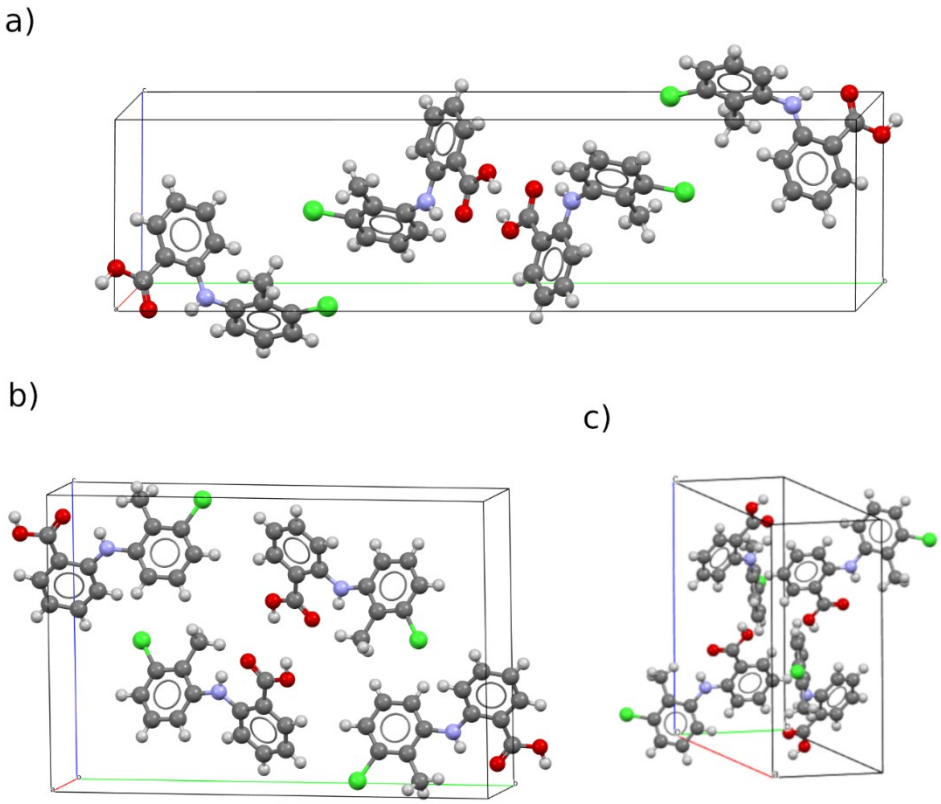

Figure S1. Crystal packing of (a) TFA-I, (b) TFA-II and (c) TFA-IX. Unit cell axes are not drawn in scale.

3. Crystal morphology of TFA-I, TFA-II and TFA-IX

The crystal morphologies of TFA-I and TFA-IX were indexed from single-crystal X-ray diffraction data. The facet displayed by the experimental morphology of TFA-I matched the indices of the morphology calculated with the BFDH method.[12] Given the similarity between the crystal structures of TFA-I and TFA-II and the facet indices of their predicted morphologies, the indices of TFA-II were assigned by comparison with TFA-I. The BFDH, attachment energy morphologies and experimental morphologies of TFA-I, TFA-II and TFA-IX are shown in Figures S2,S4 and S5, respectively. For TFA-IX there was a considerable difference between the experimental morphologies and the BFDH morphology. The latter is thus not shown. Figures S3 and S6 show the indexed experimental morphologies of TFA-I and TFA-IX, respectively.

For TFA-IX, two experimental morphologies were found in the same batch. Crystals displaying the {211} facets (experimental morphology 1) were only a few, and only crystal seeds with the simpler experimental morphology 1 were used for the experiments presented in this work, although the other experimental morphology is reported here for completeness.

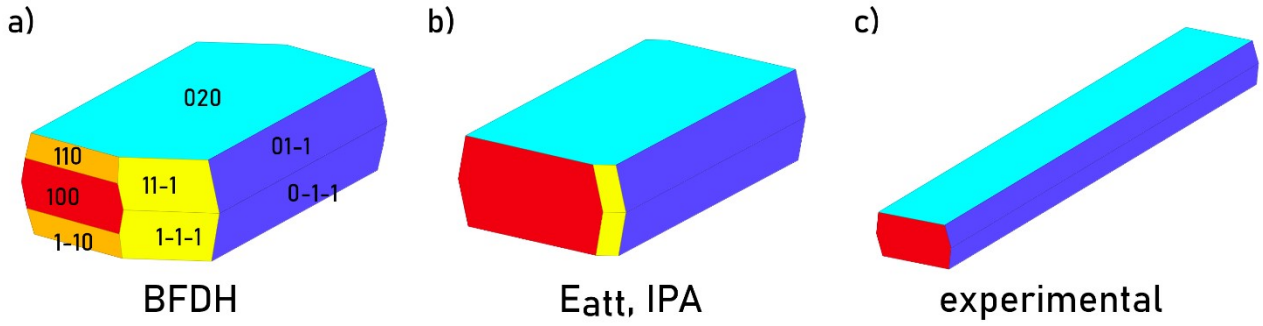

Figure S2. (a) BDFH (b) implicit IPA attachment energy and (c) experimental morphologies of TFA-I.

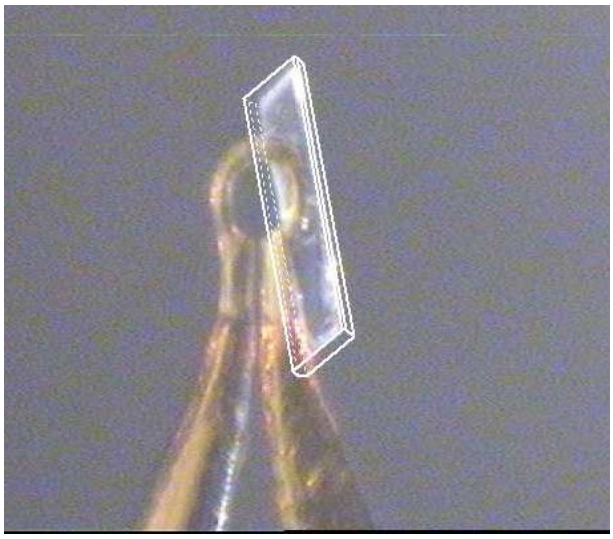

Figure S3. Indexed morphology of TFA-I

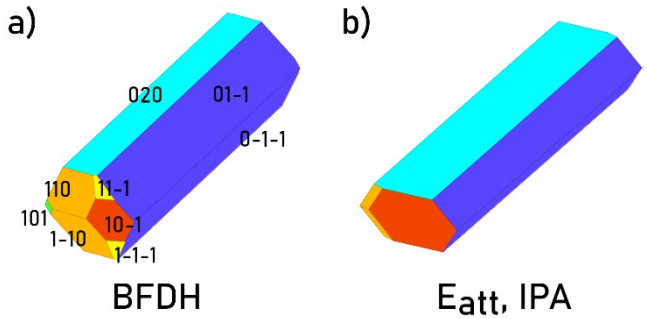

Figure S4. (a) BDFH and (b) implicit IPA attachment energy of TFA-II.

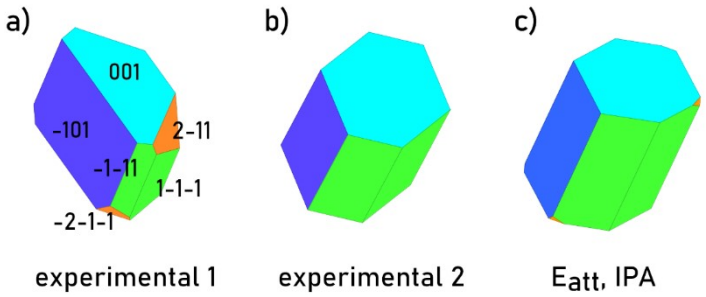

Figure S5. Experimental (a and b) and implicit IPA attachment energy (c) morphologies of TFA-IX.

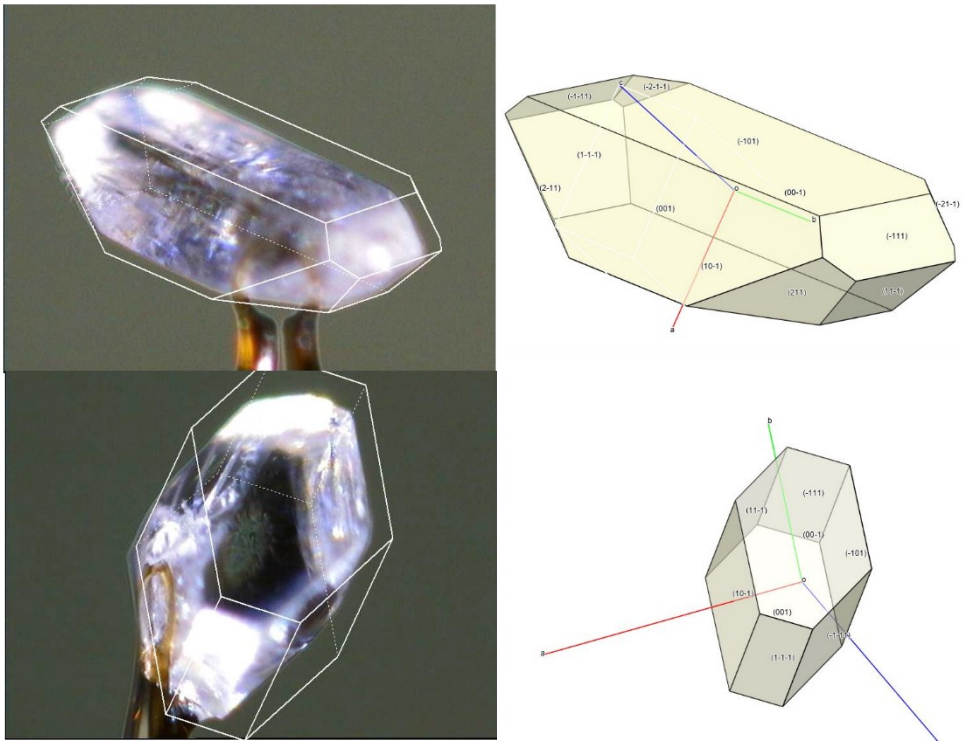

Figure S6. Indexed morphologies of TFA-IX

4. Calculation of DFT-d attachment energies

Periodic dispersion-corrected DFT was used to calculate attachment energies for relevant families of {*hkl*} planes as the difference between the lattice energy and a slice of thickness d_{hkl}. All calculations were performed using VASP 5.4.4[13–16] with the PBE functional[17] and PAW[18,19] pseudopotentials.

First, the experimental CSD[20] crystal structures KAXXAI01 (form I), KAXXAI (form II) and KAXXAI11 (form IX) were optimised with tight convergence settings (EDIFF 10^{-8}) using the Tkatchenko-Scheffler (TS) dispersion correction,[21] allowing the relaxation of both unit cell parameters and atomic positions. Single-point energy calculations were performed on the optimised structures using the many-body dispersion correction (MBD)[22,23] and divided by the number of molecules in the unit cell, Z, to obtain the electronic energy of a molecule in the crystal (E_{crys}). The lattice energy was then calculated as the difference between the energy of the molecule in the bulk crystal and the energy of an isolated gas-phase molecule ($E_{latt} = E_{crys} - E_{mol,gas}$), which was obtained by calculating the single-point MBD energy of a TFA molecule ($E_{mol,gas}$) after optimisation in a vacuum supercell of 30 Å x 30 Å x 30 Å.

Slabs parallel to the *hkl* facets of interest and having thickness d_{hkl} were generated from the optimised crystal structures and separated by vacuum slabs of about 40 Å to generate periodic supercells, for which the single-point MBD-corrected electronic energy was calculated. The energy of a molecule in the slice ($E_{slice,hkl}$) was obtained by dividing the total slab electronic energy by the number of molecules in the slab and subtracting the energy of the gas-phase isolated molecule. Finally, the attachment energies were calculated as the difference between the lattice energy and the slice energy:

$$E_{att,\{hkl\}} = E_{latt} - E_{slice,\{hkl\}} \quad \text{(S1)}$$

The effect of solvent (IPA) on the attachment energies was implicitly simulated by including the presence of a dielectric continuum using the VASPsol[24,25] module. The solvent can be specified by defining its dielectric constant ε; for this work, the values of ε were taken from the Gaussian[26] web page http://gaussian.com/scrf/.

In the case of TFA-I and TFA-II, the BFDH morphologies were generated using the CCDC software Mercury[27] to identify lists of morphologically relevant facets, and the attachment energies of the latter were calculated. In the case of TFA-IX, the calculated BFDH morphology and the experimental indexed morphology differed substantially, and therefore only the attachment energies for the facets appearing in the experimental morphologies were calculated. The calculated attachment energies were used to generate the corresponding crystal morphologies using the Wulff construction.[28] Table S3 reports the calculated attachment energies, together with the total morphological importance (i.e., the fraction of total surface) of the corresponding family of {hkl} facets.

Table S3. Calculated attachment energies for relevant crystal facets of TFA polymorphs.

					Vacuum (ε = 1)		IPA (ε = 19.3)	
Form	**Planes**	**M**[a]	**d_{hkl} / Å**	**Growth direction**	**$E_{att,\{hkl\}}$ / kJmol^{-1}**	**M. I.**[b]	**$E_{att,\{hkl\}}$ / kJmol^{-1}**	**M. I.**
TFA-I	{020}	2	16.09	T	-19.6	0.57	-19.1	0.57
	{011}	4	7.57	W	-44.1	0.28	-42.0	0.28
	{100}	2	4.55	L	-77.3	0.15	-76.2	0.13
	{110}	4	4.50	L	-98.3	0	-89.6	0.02
	{11-1}	4	4.39	L	-102.2	0	-93.0	0
TFA-II	{020}	2	10.95	T	-21.2	0.39	-19.3	0.40
	{011}	4	11.94	W	-28.6	0.48	-26.9	0.47
	{10-1}	2	3.68	L	-80.6	0.12	-81.9	0.11
	{110}	4	3.68	L	-88.1	0.01	-88.5	0.02
	{11-1}	4	3.63	L	-103.9	0	-97.4	0

	{100}	2	3.84	L	-124.8	0	-110.5	0
	{101}	2	3.55	L	-129.7	0	-114.1	0
TFA-IX	{10-1}	2	9.14	-	-34.3	0.36	-34.4	0.33
	{001}	2	14.54	-	-50.6	0.32	-41.5	0.36
	{11-1}	4	5.92	-	-61.1	0.32	-59.8	0.31
	{211}	4	3.90	-	-100.2	0.00	-84.2	0.00

[a] facet multiplicity; [b] morphological importance

Regardless of the known limitations of the attachment energy model, according to which growth rates are directly proportional to calculated attachment energies and which does not consider the effect of different growth mechanisms or of the growth environment, there is a fairly good agreement between experimental and predicted growth rates of TFA if these are compared qualitatively. In the case of TFA-IX, the calculated attachment energies of all facets have intermediate values between the attachment energies of the facets growing in the L direction of TFA-I and TFA-II and those growing in the W direction. In addition, the relative order of the predicted growth rates of TFA-IX follows that of its experimental perpendicular facet growth rates (see Figure S24). For TFA-I and TFA-II, the predicted growth rates are faster for the facets growing in the L direction than those in the W direction, although their relative dimension is heavily underestimated compared to our measured values. Since the attachment energy model assumes layer-by-layer growth of crystal facets this is not surprising given the peculiar growth mechanism we observed for these needle crystals (see main text).

5. Crystal growth rates of TFA polymorphs from single-crystal data

5.1. Measurement of linear growth rates in stagnant growth cell

Linear growth rates of single-crystal seeds were measured in a stagnant growth cell[29] where crystals are placed inside a cuvette filled with solution of known concentration. The growth of the crystal seeds is monitored by recording images of the growing crystals at set intervals of time (varying between 6 to 20 seconds between frames for this work). In this technique, the solution supersaturation is assumed constant and only slightly affected by the growth of the crystal seed for the whole duration of the experiments. This was verified by estimating the change in supersaturation over the course of 120 minutes (typical duration of our experiments) for the TFA polymorphs using their mass growth rates, converted from volume growth rates using the crystal's density. Over 120 minutes, a supersaturation decrease of only 0.5% was calculated using the highest overall volume growth rate (TFA-IX, σ=0.3, see Section 5.12). Another assumption is that the increase in supersaturation due to the dissolution of crystal seeds before the experiment is small, as verified in a previous work.[6]

The needle crystals of TFA-I and TFA-II were positioned in the growth cell so that they would sit on the dominant {020} faces. Their linear growth rates were estimated by considering the time-dependent change of the *length* (L) and *width* (W) dimensions of each crystal, which for both polymorphs correspond to the directions parallel to the crystallographic *a* ([100] direction) and *c* axes ([001] direction), respectively. All images were processed in MATLAB and the relevant crystal dimensions were extracted by calculating the minimum area bounding box[30] (Figure S7) of each *crystal object* after pre-processing (conversion to grey-scale image and conversion to binary image). The linear growth rates were then calculated as the slope of the best-fit line for the relevant dimension vs. time data (Figure S7).

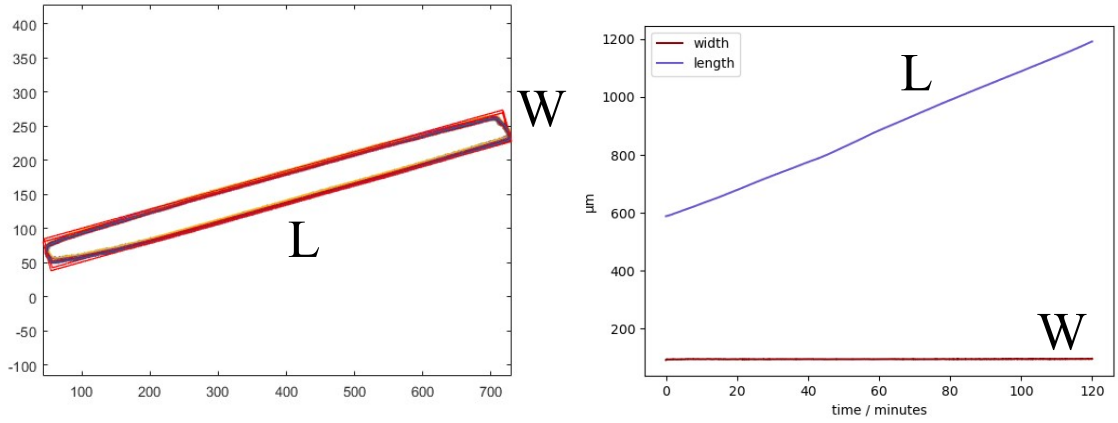

Figure S7. The length and with dimensions of needle crystals were measured from collected images by constructing a minimum area bounding box in MATLAB (left). The slope of the length vs. time data yields linear growth rates (right).

For TFA-IX crystal seeds were measured in two different orientations (Figure S8). In orientation A, the crystal seeds were positioned on their {001} facets, while they were positioned on the {10-1} facets in orientation B. Linear growth rates for specific crystal facets were obtained by measuring the corresponding centroid-edge distances using a method developed in our group (Figure S9).[31] In orientation A, the edges of the two {10-1} facets and those of the four {11-1} facets were measured. In orientation B, the edges of the two {001} facets and the edges corresponding to the common growth front of the {11-1} facets were measured. The measured centroid-edge distances for TFA-IX were converted into perpendicular facet distances to calculate facet-specific growth rates and to model the morphology of the TFA-IX crystals during growth. The corrections applied to the centroid-facet distances are discussed in Section 5.4.

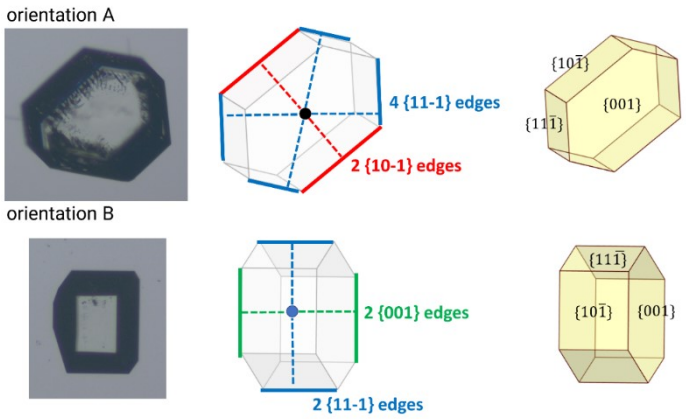

Figure S8. The two orientations in which the crystal seeds of TFA-IX were measured. The crystal facet indices were assigned from the images (left and middle), and the distance of the corresponding edges (l_i, not all are shown in the figure) from the crystal centroid (C') were measured. 18 crystal seeds with orientation A and 5 with orientation B were measured.

Figure S9. (Left) a greyscale image of a crystal of TFA-IX collected during experiments. (Right) The same image after binarization, edge detection and measurement.

With the exception for the W direction in the needle-crystals of TFA-I and TFA-II, the measured distance vs. time data showed a good linearity over the whole duration of experiments (Figure S11 and Figure S12) for all of the crystal seeds measured. In the case of the W dimension of both TFA-I and TFA-II, the fits were often poor. This was an effect of the small growth rates for this direction for both polymorphs: the change of the W dimension between consecutive image frames was often smaller than one pixel (0.86 μm), causing inconsistencies in the detection of the boundaries of the crystal object during image processing. For TFA-I three experiments resulted in negative correlation coefficients for the W dimension vs. time data (Figure S10), although no actual dissolution of the crystals for this direction was observed. We believe that manual measurement of the same dimension would result in analogous oscillations. In this case, the growth rate of the W dimension was set to zero, although its error was calculated normally.

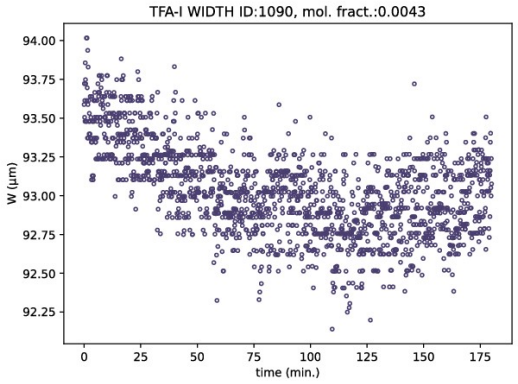

Figure S10. Oscillation of the W dimension for a crystal seed of TFA-I. The oscillations are due to limitations of the crystal edge identification by the image-processing code when the growth of the crystal is barely detectable.

For TFA-I, the growth rates of 35 crystal seeds at six different supersaturation levels were measured. For TFA-II the measured seeds were 26, and the supersaturation levels were five. For TFA-IX 23 crystal seeds at five supersaturation levels were measured. Quantities corresponding to the same supersaturation level were grouped, and the error on their average was calculated as described in Section 7.5.

Crystals of TFA-I and TFA-II grew with a peculiar mechanism which is discussed in the main text. Briefly, individual parallel micro-sized needles were observed to grow aligned with the crystal needle axis. This behaviour was observed for several crystals of both TFA-I and TFA-II grown in IPA solutions, including the case of a very large crystal, which was left in an IPA solution for six months. This crystal, visibly composed of several *fragments*, showed the same pleochroic response when analysed with a polarising microscope (Figure S13).

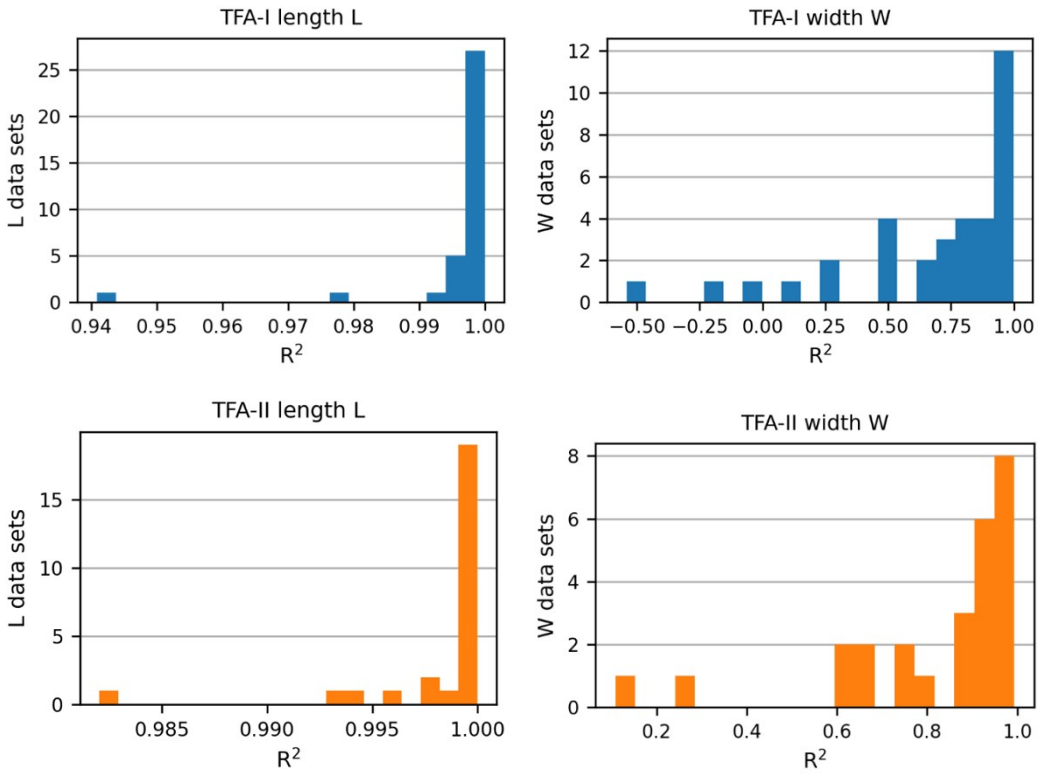

Figure S11. Histograms showing the distributions of the distance-time correlation coefficient for the L and W dimensions of TFA-I (blue, 35 crystals) and TFA-II (orange, 26 crystals).

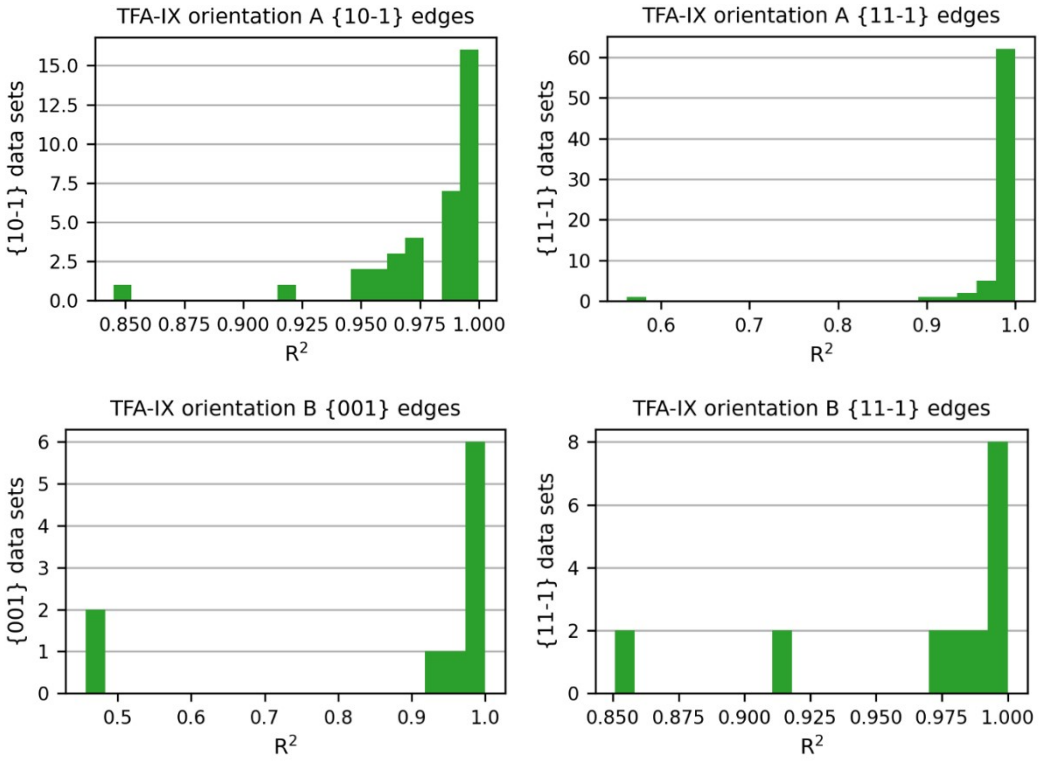

Figure S12. Histograms showing the distributions of the distance-time correlation coefficient for the centroid-edge distances for 23 crystals of TFA-IX in both orientation A (top, 18 crystals) and B (bottom, 5 crystals).

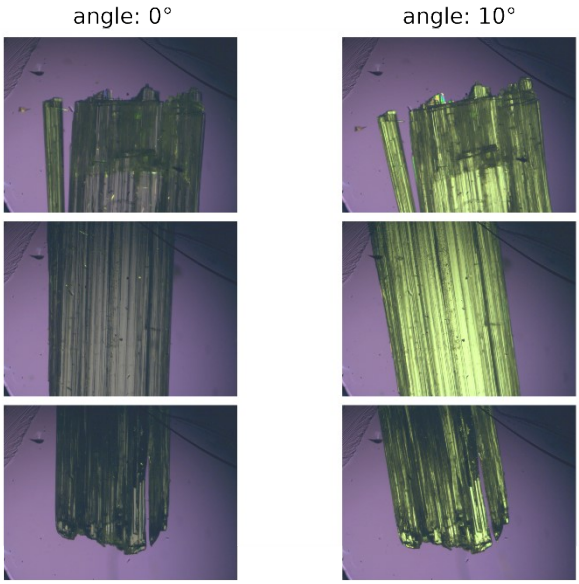

Figure S13. Images of a large crystal of TFA-I grown in IPA obtained with a polarising microscope after a rotation of 10°. Due to the large size of the crystal along the needle direction, only images of the top, middle and bottom portions of the crystal are shown. The width of the crystal was of about 2 mm.

5.2. Volumetric shape approximation for TFA-I and TFA-II

The volumetric growth of TFA-I and TFA-II crystals can be related to the measured linear dimensions by approximating their 3D shape with either a cylinder of height L and diameter W or a box of sides L, W and T. The two former dimensions (L and W) can be directly measured from the images collected from experiments, although estimating the thickness T for a box shape approximation requires some assumptions, as this cannot be measured directly, unlike for TFA-IX (see the next Section).

For our analysis as presented in the main text and in Sections 5.11, 5.12 and 5.14 of this document, we have decided to approximate the shape of needle crystals of TFA-I and TFA-II using a cylindrical shape, thus removing the need to make any assumption concerning their thickness. An alternative approach using box shapes is briefly discussed in Section 5.13.

5.3. Estimation of the height of TFA-IX crystals

To calculate perpendicular facet distances from the measured centroid edge distances, knowledge of the TFA-IX crystals height is required, as is shown in the next Section. For both the orientations A and B used for our measurements, this dimension can be estimated from collected images by measuring the projection L_{xy} of the oblique facets on the facets parallel to the image plane (Figure S14). For orientation A, these are the projections of the {10-1} facets on the {001}, and vice versa

for orientation B. Using this projection, the height can be calculated from each image at time *t* using the interfacial angle θ as:

$$H(t) = L_{xy}(t)tan\theta \quad \text{(S2)}$$

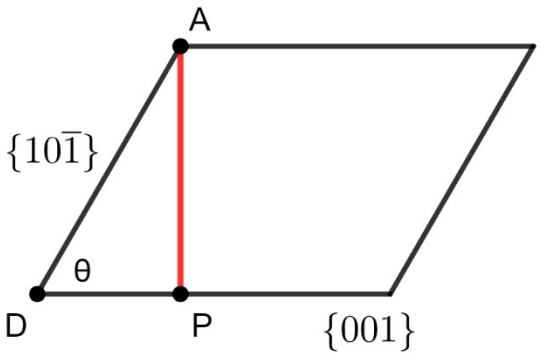

Figure S14. The height of TFA-IX crystals (segment AP) can be calculated from 2D images by measuring the length of the projection DP. The shape in the figure represents a crystal in orientation A viewed from the side.

For crystals in orientation A, the height corresponds to twice the perpendicular distance of the {001} facets, while it corresponds to twice the {10-1} distance in case of orientation B.

Particular attention was required in the case of TFA-IX crystals measured in orientation A. In this orientation, with the crystallographic *b* axis is parallel to the image plane, the light passing through the crystal is refracted, and two different projections can be measured (Figure S15). Either a "right" projection *l'*, a "wrong" projection *l''* or both can be present depending on the rotation of the crystal around the microscope's optical axis. The range of rotational angles for which only *l''* was visible was identified and crystals in orientations falling in this range were not measured.

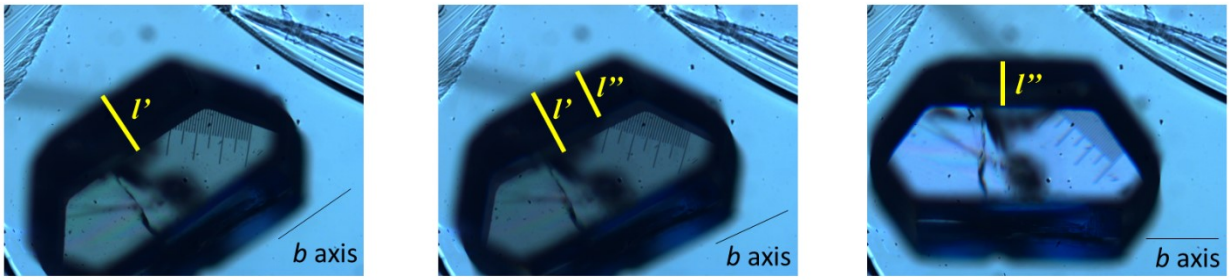

Figure S15. Effect of the optical birefringence distortion on the measured projection of the oblique facets in a crystal of TFA-IX. When no distortion is present (left) the measurement of *l'* yields the correct crystal height. When the crystal is rotated by 15° (middle), a second projection, *l''*, appears. If the crystal is rotated further (+ 30°, right), the projected dimension *l'* disappears, the crystal goes out of focus, and the height calculated using *l''* and equation S6 underestimated.

If the "wrong" projection *l''* is used in equation S6, the height of the TFA-IX crystals can be underestimated by about 100-150 µm. If the "right" projection *l'* is used, instead, crystal heights within 30 µm can be determined. This was verified by measuring crystals of TFA-IX using both laser confocal microscopy and a chromatic confocal sensor (Figure S16) and comparing the results with values estimated using equation S2.

To calculate the height of TFA-IX crystals, one every third image from each collected data set was manually modified as shown in Figure S17. The modified images were then processed using the same code used to measure the needle crystals of TFA-I and TFA-II. The heights for the remaining images were calculated by interpolation.

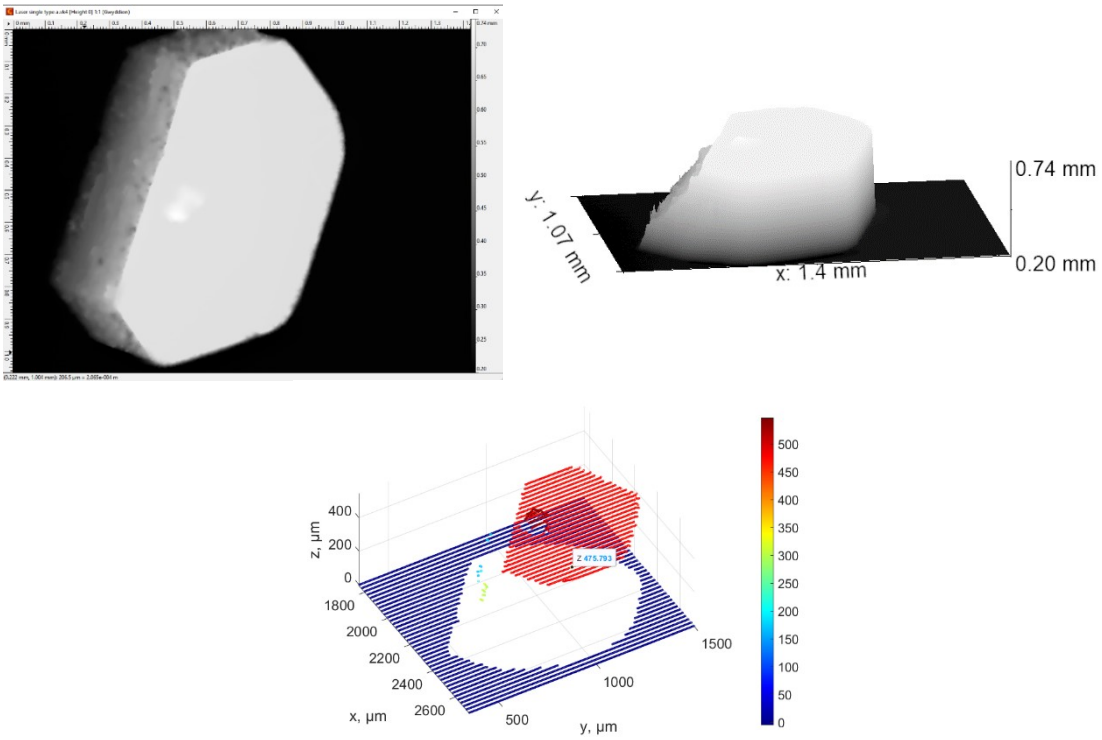

Figure S16 Laser confocal microscopy and a chromatic confocal sensor were used to measure the height of TFA-IX crystals and compare the results with values calculated using eq. S6.

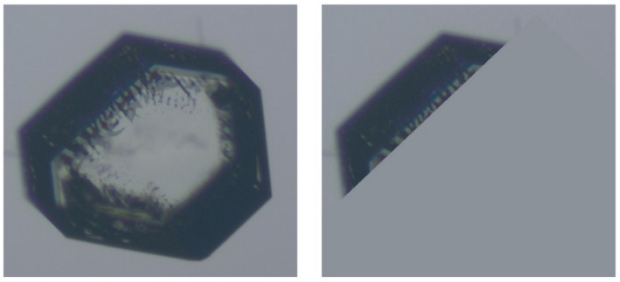

Figure S17. Images of TFA-IX crystals collected during experiments were manually modified to calculate the height of the crystals using eq. S2.

5.4. Transformation of centroid-edge distances in facet-specific distances for TFA-IX crystals

The blocky morphology of the TFA-IX crystals suggest that growth rates of similar magnitude should be expected for all visible crystal facets. In such case, the change of a measured centroid-edge distance between an image collected at time *t* and an image collected at time *t+1* will depend on contributions from the normal growth rates of the two crystal facets that form the edge, as shown in Figure S18.[32,33]

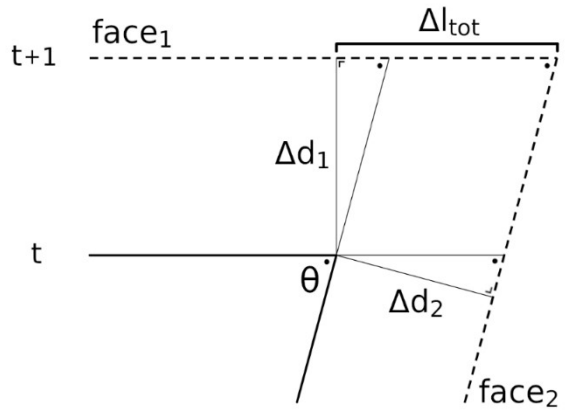

Figure S18. Contribution of facet normal growth rates on the change in centroid-edge dimension change Δl_{tot}. In this view, the facet denoted with $face_1$ can represent the {001} facets of a crystal of TFA-IX measured in orientation A.

The total distance change between two consecutive images will be given by:

$$\Delta l_{tot} = \Delta l_1 + \Delta l_2 = \Delta d_1 \frac{cos\theta}{sin\theta} + \Delta d_2 \frac{1}{sin\theta} \quad \text{(S3)}$$

And the change of the perpendicular facet distance can thus be calculated as:

$$\Delta d_2 = \Delta l_{tot} sin\theta - \Delta d_1 cos\theta \quad \text{(S4)}$$

Using the construction shown in Figure S19, an equation analogous to eq. S4 can be found to relate the perpendicular facet distance to the centroid-edge distances, $D_{edge,(hkl)}(t)$, measured for each image at time *t*:

$$d_{(hkl)}(t) = D_{edge,(hkl)}(t) sin\theta - \frac{H(t)}{2} cos\theta \quad \text{(S5)}$$

Where H(t) is the crystal height as calculated with eq. S2. Equation S5 was used to calculate normal facet distances for {10-1} and {11-1} facets for crystals with orientation A and the {001} facet distances for crystals with orientation B.

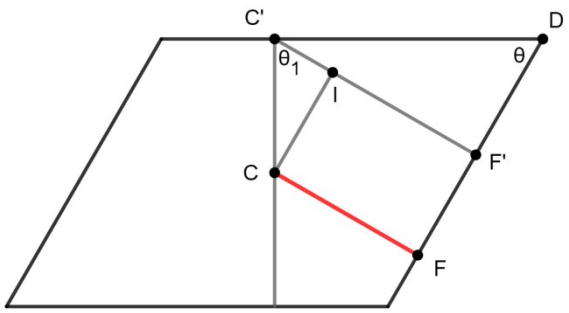

Figure S19. The geometric construction used in equation S9 to calculate the facet distance (CF) starting from the measured centroid-edge distance (C'D) for the {10-1} and {11-1} facets in crystals with orientations A and for the {001} facets in crystals with orientation B. In this figure, the crystal is viewed from the side.

For crystals in orientation B the distance of the {11-1} facets, $d_{\{11\text{-}1\}}$, was calculated as:

$$d_{\{11-1\}} = D_{edge,\{11-1\}}(t)sin\kappa \quad \text{(S6)}$$

Where κ is half of the interfacial angle between two adjacent facets of the {11-1} family (Figure S20). This method assumes that pairs of adjacent {11-1} facets always have the same distance from the centre, and thus identical growth rates.

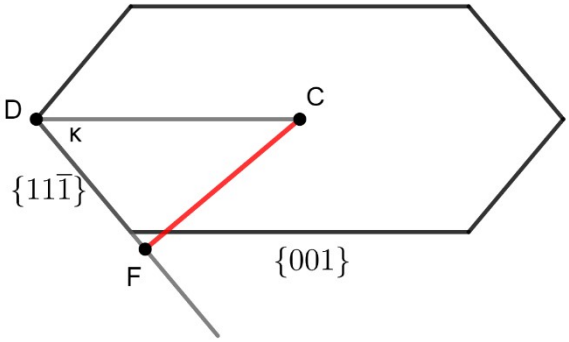

Figure S20. Geometric construction used to deduce the perpendicular distance (CF) of the {11-1} crystal facets from the measured centroid-edge distance (CD) for crystals with orientation B.

The quality of our approximation of the crystal height of TFA-IX crystals, as well as the validity of the mathematical corrections applied to the measured distances were evaluated qualitatively by overlapping collected images of TFA-IX crystals to the 2D projections of their 3D morphologies, calculated using facet distances obtained as described above (Figure S21). We note that, while our approach worked well for the crystals of TFA-IX presented here, the applicability of this method, as well as the corrections needed to convert the growth cell distances to crystal facet distances, will depend on the system studied.

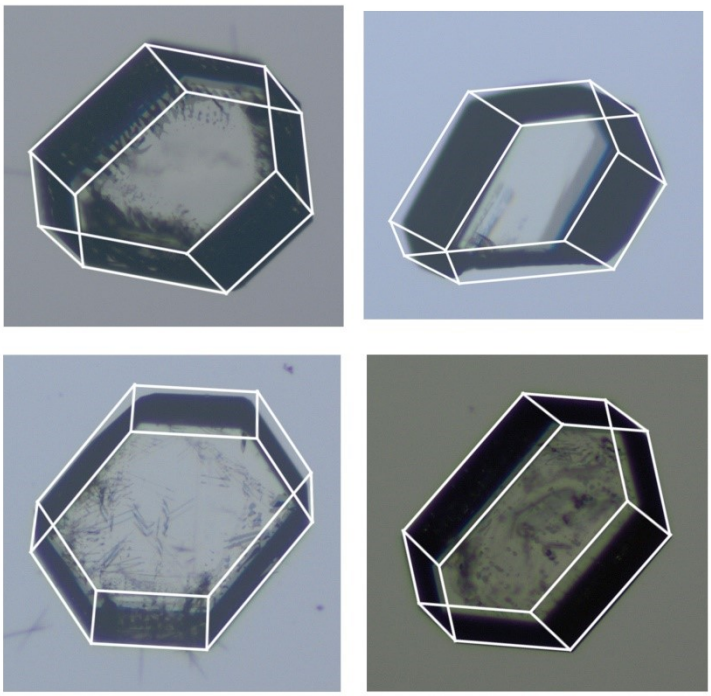

Figure S21. Overlay of experimental images and the 2D projections of 3D crystal morphologies calculated from facet-distances obtained by measurements of crystal dimensions as described in this section.

5.5. Linear growth rates of TFA polymorphs

The average linear growth rates from our measurements of single crystals of TFA-I, TFA-II and TFA-IX in IPA at 25 °C are reported in Tables S4 and S5 together with the associated standard deviations. The latter were calculated as described in Section 7. The growth rates of the L and W directions are reported for TFA-I and TFA-II. For TFA-IX, the growth rates of the measured centroid-edge dimensions, as well as the corrected perpendicular growth rates of the {001}, {10-1} and {11-1} facets are reported. The latter were calculated applying the geometrical corrections described in Section 5.4.

Table S4. Average single-crystal growth rates of TFA-I and TFA-II in IPA at 25 °C. The coefficients of variation of the [100] growth rates are also reported.

TFA-I (35 crystals)		**Growth rate**	**Var. coeff. [100]**	**Growth rate**
x **(x10^{-3}) / mol. fraction**	**σ_I**	**$G_{[100]}$ (µm min^{-1})**	**$\sigma/\bar{x}$**	**$G_{[001]}$ (µm min^{-1})**
4.33 ± 0.01	0.10	0.3 ± 0.1	0.29	0.001 ± 0.003
4.70 ± 0.02	0.20	0.8 ± 0.2	0.22	0.018 ± 0.006
5.07 ± 0.05	0.29	1.8 ± 0.2	0.11	0.006 ± 0.004
5.47 ± 0.01	0.39	2.8 ± 0.3	0.14	0.01 ± 0.01

5.86 ± 0.04	0.49	4.5 ± 0.5	0.20	0.03 ± 0.02
6.24 ± 0.01	0.59	4.3 ± 0.5	0.13	0.05 ± 0.03
TFA-II (26 crystals)		**Growth rate**	**Var. coeff. [100]**	**Growth rate**
x **(x10^{-3}) / mol. fraction**	**σ_{II}**	**$G_{[100]}$ (µm min^{-1})**	**$\sigma/\bar{x}$**	**$G_{[001]}$ (µm min^{-1})**
4.82 ± 0.06	0.12	1.3 ± 0.2	0.14	0.012 ± 0.008
5.10 ± 0.01	0.19	2.2 ± 0.7	0.34	0.016 ± 0.020
5.48 ± 0.01	0.28	4.2 ± 0.4	0.10	0.016 ± 0.013
5.84 ± 0.03	0.36	7.2 ± 1.7	0.25	0.041 ± 0.021
6.24 ± 0.02	0.45	20.8 ± 2.0	0.11	0.078 ± 0.033

Table S5. Average single-crystal growth rates of TFA-IX in IPA at 25 °C.

TFA-IX (23 crystals)	**Centroid-edge growth rates**				
x **(x10^{-3}) / mol. fraction**	**σ_{IX}**	**Orientation A {10-1} edges**	**Orientation A {11-1} edges**	**Orientation B {11-1} edges**	**Orientation B {001} edges**
5.03 ± 0.03	0.05	0.07 ± 0.02	0.10 ± 0.05	0.06 ± 0.01	0.05 ± 0.01
5.48 ± 0.02	0.14	0.11 ± 0.02	0.14 ± 0.04	0.09 ± 0.01	0.12 ± 0.01
5.88 ± 0.03	0.22	0.16 ± 0.05	0.27 ± 0.09	0.20 ± 0.01	0.22 ± 0.01
6.05 ± 0.02	0.26	0.27 ± 0.03	0.44 ± 0.05	-	-
6.25 ± 0.02	0.30	0.50 ± 0.11	0.48 ± 0.10	-	-
TFA-IX (23 crystals)	**Corrected perpendicular facet growth rates**				
x **(x10^{-3}) / mol. fraction**	**σ_{IX}**	**$G_{\{001\}}$ / µm min^{-1}**	**$G_{\{10\text{-}1\}}$ / µm min^{-1}**	**$G_{\{11\text{-}1\}}$ / µm min^{-1}**	
5.03 ± 0.03	0.05	0.04 ± 0.02	0.10 ± 0.06	0.07 ± 0.04	
5.48 ± 0.02	0.14	0.10 ± 0.01	0.08 ± 0.02	0.10 ± 0.03	
5.88 ± 0.03	0.22	0.26 ± 0.10	0.11 ± 0.04	0.21 ± 0.08	
6.05 ± 0.02	0.26	0.32 ± 0.04	0.17 ± 0.02	0.38 ± 0.04	
6.25 ± 0.02	0.30	0.37 ± 0.25	0.36 ± 0.10	0.40 ± 0.08	

5.6. Evaluation of the growth mechanism

The dominant growth mechanism responsible for the growth of specific crystal directions can be identified by describing the effect of supersaturation on growth rates using common growth mechanism models and evaluating if any of the tested models is successful in describing the experimental data.[34–36]

The normal growth of a crystal facet proceeds by the consecutive addition of layers and its growth rate G_{hkl} is given by:

$$G_{hkl} = \left(\frac{h}{\tau}\right)_{hkl} \tag{S7}$$

Where h is the layer or step height and τ is the time required for the completion of a layer (i.e., for the full coverage of the facet). The growth across a layer proceeds through the addition of new growth units to special step and kink surface sites. At low supersaturation, the only source of these special sites are crystal dislocation defects, and the growth rate of a facet is described by the Burton, Cabrera and Frank (BCF) or *spiral growth* model:[37]

$$G_{BCF} = A\frac{\sigma^2}{B}tanh\left(\frac{B}{\sigma}\right) \tag{S8}$$

As the supersaturation increases, *growth islands* can spontaneously form on the crystal surface and provide the necessary sites for the layer growth. Under this growth regime, growth rates can be described by the two-dimensional or Birth and Spread (BS) model.[38] When the growth of a crystal facet proceeds through the BS mechanism, its growth rate is described by:

$$G_{BS} = C\sigma^{5/6}exp\left(\frac{-D}{\sigma}\right) \tag{S9}$$

For high enough supersaturations multiple islands can form and provide additional growth sites and causing the surface to become *rough.* In a *rough growth* regime, the growth rate depends linearly on supersaturation through a rate constant:

$$G_{linear} = k_{linear}\sigma \tag{S10}$$

In alternative, growth rates are commonly represented by the empirical power law expression:

$$G_{pow} = k_1\sigma^g \tag{S11}$$

Where the exponent g commonly assumes values between 1 and 2.

In these equations the supersaturation is expressed for each polymorph *i* as:

$$\sigma_i = \frac{x - x_i^*}{x_i^*} \tag{S12}$$

Where x and x_i are the solution concentration and the equilibrium solubility, respectively.

The growth models mentioned above were fitted to experimental data using a weighted least-squares approach where weights were assigned according to experimental errors.

5.7. Fitted growth models for TFA-I and TFA-II

The parameters obtained by fitting the growth models presented above are reported in Table S6 and Table S7 and plotted in Figures S22 and S23 for TFA-I and TFA-II, respectively.

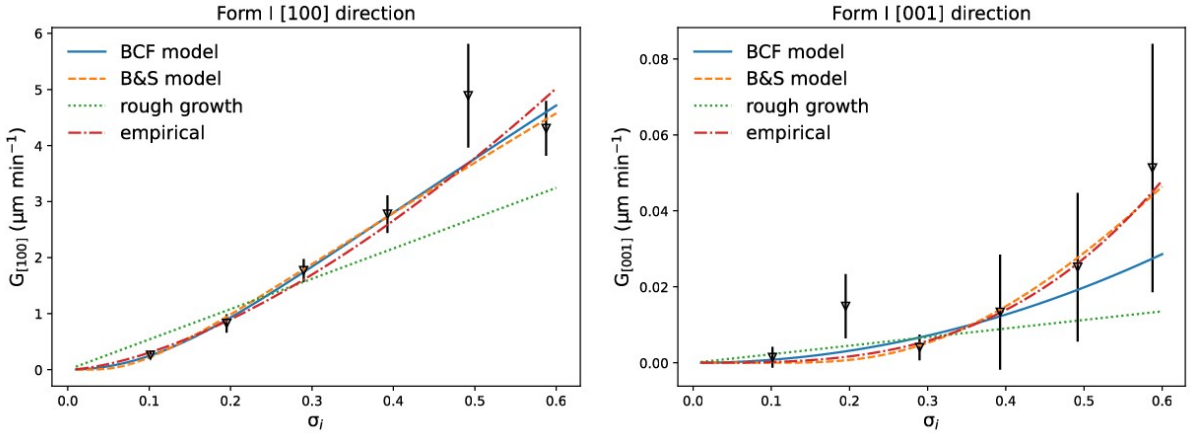

Figure S22. Experimental average growth rates of the L (left) and W (right) dimensions in IPA at 25°C for TFA-I crystals and fitted growth models. The fitted parameters are reported in Table S6.

Table S6. Fitted parameters, coefficients of determination and sum of squared residuals (ssr) for the experimental linear growth rates of TFA-I.

TFA-I				
BCF	**A (µm min^{-1})**	**B**	**R^2**	**SSR**
[100] direction	8.6	0.4	0.911	1.54
[001] direction	2.1	26	0.546	0.0008
BS	**C (µm min^{-1})**	**D**	**R^2**	**SSR**
[100] direction	9.5	0.2	0.905	1.65
[001] direction	0.35	1.0	0.841	0.0002
Continuous	**k_{linear} (µm min^{-1})**	**-**	**R^2**	**SSR**
[100] direction	5.4	-	0.610	6.84
[001] direction	0.02	0	-0.073	0.002
Power law	**k_1 (µm min^{-1})**	**g**	**R^2**	**SSR**
[100] direction	11.2	1.6	0.894	1.84
[001] direction	0.23	3.1	0.867	0.0002

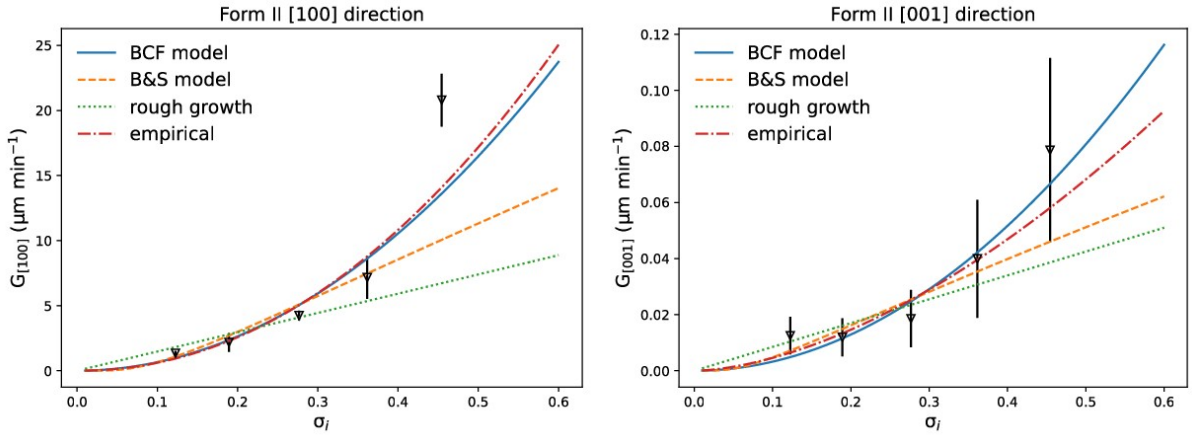

Figure S23. Experimental average growth rates of the L (left) and W (right) dimensions in IPA at 25°C for TFA-II crystals and fitted growth models. The fitted parameters are reported in Table S7.

Table S7. Fitted parameters, coefficients of determination and sum of squared residuals (ssr) for the experimental linear growth rates of TFA-II.

TFA-II				
BCF	**A (µm min^{-1})**	**B**	**R^2**	**SSR**
[100] direction	337.8	5.12	0.784	54.5
[001] direction	5.62	17.4	0.923	0.0002
BS	**C (µm min^{-1})**	**D**	**R^2**	**SSR**
[100] direction	29.4	0.2	0.540	116.4
[001] direction	0.1	0.1	0.635	0.001
Continuous	**k_{linear} (µm min^{-1})**	**-**	**R^2**	**SSR**
[100] direction	14.8	-	0.202	201
[001] direction	0.1	-	0.459	0.001
Power law	**k_1 (µm min^{-1})**	**g**	**R^2**	**SSR**
[100] direction	72.1	2.1	0.809	48.4
[001] direction	0.2	1.7	0.842	0.001

5.8. Fitted growth models for TFA-IX

The optimised parameter of selected growth models for TFA-IX are reported in Table S8, while the fits are represented in Figure S24.

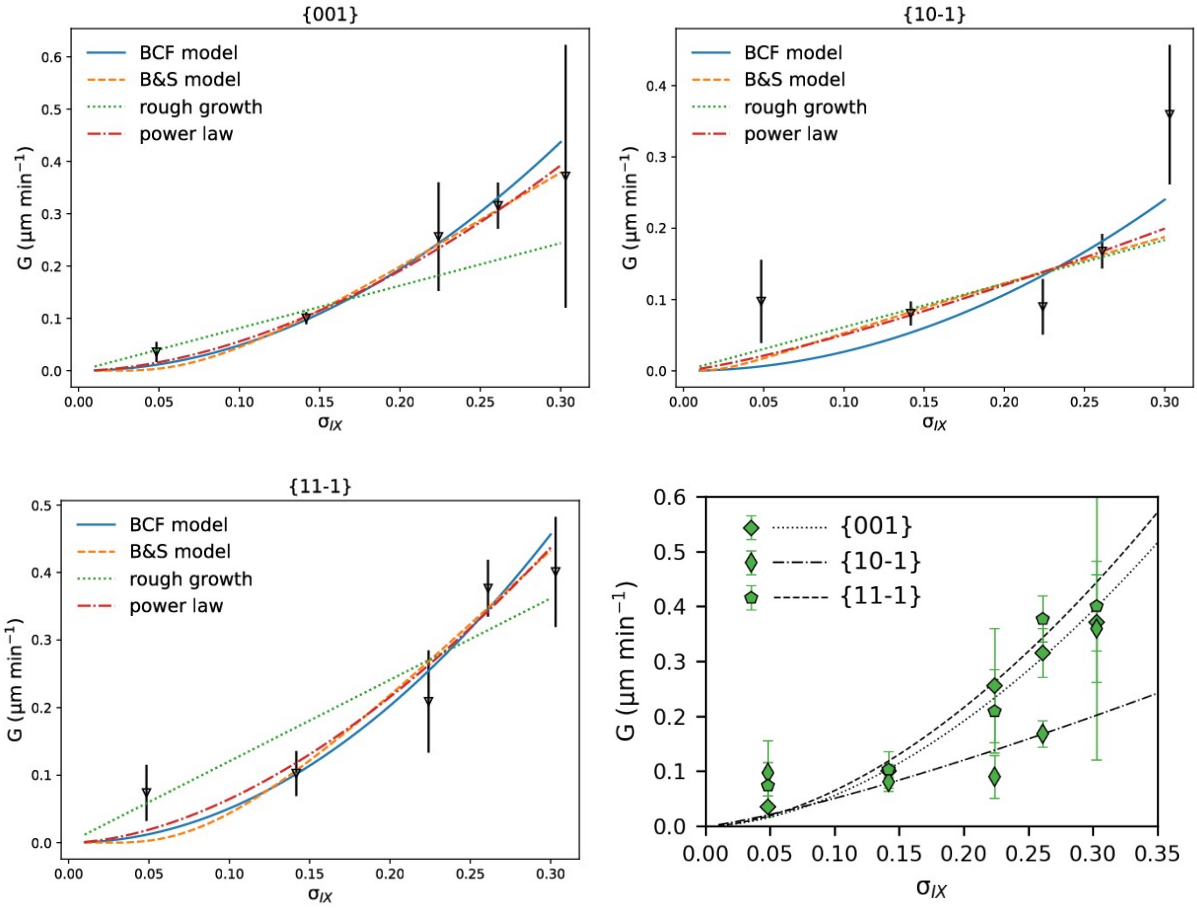

Figure S24. Experimental average growth rates of the {001} (top left), {10-1} (top right) and {11-1} (bottom left) facets in IPA at 25°C for TFA-IX crystals and fitted growth models. The growth rates of the three facets are compared in the bottom right portion of this figure, where dashed lines were obtained fitting the power law growth model. The fitted parameters are reported in Table S8.

Table S8. Fitted parameters, coefficients of determination and sum of squared residuals (ssr) for the experimental facet growth rates of TFA-IX.

TFA-IX				
BCF[a]	**A (µm min^{-1})**	**B**	**R^2**	**SSR**
{001}	22.4	4.6	0.920	0.007
{10-1}	21.8	8.2	0.559	0.024
{11-1}	20.1	4.0	0.879	0.011
BS	**C (µm min^{-1})**	**D**	**R^2**	**SSR**
{001}	1.9	0.18	0.982	0.001
{10-1}	0.6	0.05	0.314	0.038
{11-1}	2.4	0.21	0.881	0.011
Continuous	**k_{linear} (µm min^{-1})**	**-**	**R^2**	**SSR**

{001}	0.8	-	0.607	0.032
{10-1}	0.6	-	0.323	0.037
{11-1}	1.2	-	0.851	0.014
Power law	**k_1 (µm min^{-1})**	**g**	**R^2**	**SSR**
{001}	3.3	1.8	0.978	0.002
{10-1}	0.9	1.2	0.399	0.033
{11-1}	3.5	1.7	0.899	0.009

[a]fits of the BCF model are not reliable and the optimised parameters change considerably depending on the selected parameter initial values.

5.9. Calculation of crystal morphology volume: the Particle Property Calculator (PPC) algorithm

The Particle Property Calculator (PPC) was written in Python3 with the objective of calculating the evolution of the volume of crystals of TFA-IX during growth from the distance data collected during our experiments. The PPC can calculate the volume of any crystal morphology (represented by a convex polyhedron) from a crystal structure and from a list of crystal facets and their perpendicular distances. A comparison of the performance of PPC with the Morphology module of Materials Studio 2019 (BIOVIA) is provided in the next Section.

Figure S25 provides a schematic view of the process used by PPC to calculate the volume and surface of the morphology convex hull. PPC uses custom written functions, as well as functionalities of the SciPy library[39] and of the CSD python API.[20]

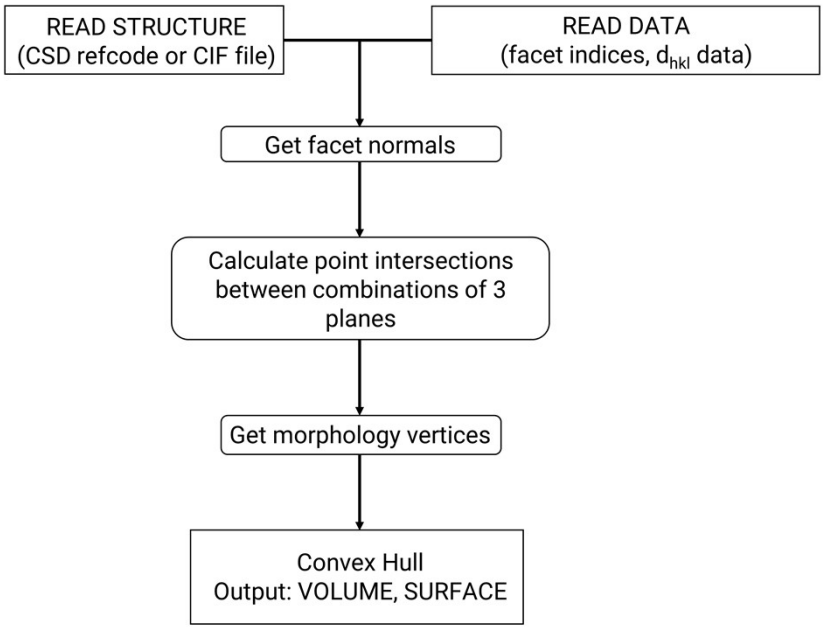

Figure S25. Schematic view of the PPC algorithm to calculate crystal morphology volume and total surface.

An input crystal structure, either read from the CSD database through its refcode or from a CIF file, is used to calculate the plane normal of each crystal facet with indices *hkl*:

$$\hat{n}_{(hkl)} = (a_{(hkl)}, b_{(hkl)}, c_{(hkl)}) \quad \text{(S13)}$$

Each crystal facet is then defined by its plane equation:

$$a_{(hkl)}x + b_{(hkl)}y + c_{(hkl)}z + d_{(hkl)} = 0 \quad \text{(S14)}$$

The perpendicular facet distances d_{hkl} can be determined from experimental observations or from computational predictions. The input distances have arbitrary units which will determine the unit of the output volume/surface.

The intersections of all combinations of three distinct planes (representing the crystal facets) are calculated only if the rank of the corresponding matrix is equal to 3, i.e., if the solution represents a point with 3D coordinates. The points identified this way will include the morphology vertices, as well as points *external* to the morphology convex hull. The latter are excluded by recursively verifying if a point lies on either the same or opposite side of a crystal facet with respect to the origin. This is done by evaluating $F_{(hkl)}(x_i,y_i,z_i)$ for each point, where $F_{(hkl)}$ is the equation of the facet plane and x_i,y_i,z_i are the coordinates of the *i*th point (Figure S26). If the point lies on the plane ($F_{(hkl)}(x_i,y_i,z_i) = 0$), or on the same side as the origin ($F_{(hkl)}(x_i,y_i,z_i) > 0$), then the point is kept. The operation is repeated for all crystal facets until only the real morphology vertices are left (Figure S27). This methodology for the search of the morphology vertices was preferred to a nearest-neighbour search based on distances between points, because the latter can result in false positives in the case of crystals with particularly acute interfacial angles. The volume and the surface of the crystal morphology are then calculated from the collection of vertices using the Quickhull algorithm.[40]

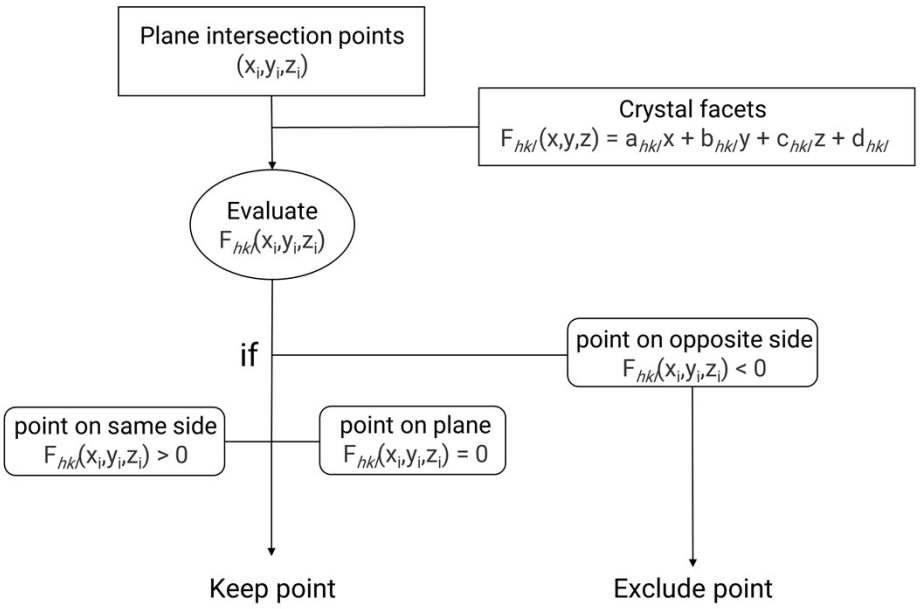

Figure S26. Schematic representation of the Nearest-Neighbour search algorithm used to find the crystal morphology vertices.

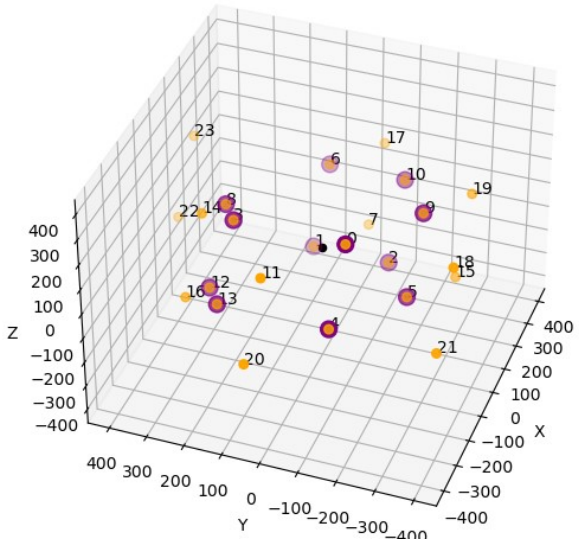

Figure S27. All possible intersection points between the crystal facets of a TFA-IX crystal (orange points) are limited to the morphology vertices (purple points) using a Nearest-Neighbour search algorithm.

5.10. Evaluation of the performance of the PPC algorithm

PPC has a comparable performance to the commercial Morphology module of Materials Studio 2019 (Dassault Systems BIOVIA, 2018). As a benchmark, the BFDH morphologies of 26 crystal structures from the CSD were calculated in Materials Studio. The Materials Studio output lists of *hkl* facets and

their corresponding distances were then used as inputs for the calculation with PPC using the same crystal structures. The parity plots for the crystal volume and surface area calculated with the two methods are shown in Figure S28.

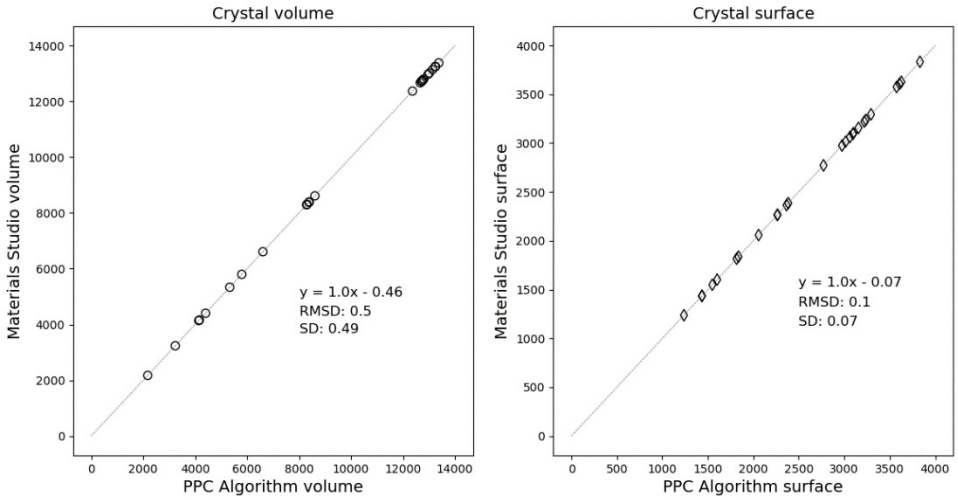

Figure S28. Comparison of the volume (left) and surface (right) calculated using the PPC algorithm presented in this work (*x* axis) and the commercial Morphology module of Materials Studio 2019 (*y* axis) for crystal morphologies of 26 selected systems The units of measurement are arbitrary and depend on the input data.

5.11. Calculation of crystal growth volumes

The change of crystal volume after a fixed time t can be used to evaluate the influence of linear growth rates on crystal volume change. This measure provides a qualitative comparison of overall growth rates of polymorphs, as used previously by Liu et al.[41]

Volume growth rates of TFA polymorphs were calculated using the average experimental growth rates measured at different concentrations. The shape of the crystals was defined using aspect ratios calculated from the average dimensions of the seeds used for our experiments (Table S11). The initial crystal volume was fixed to the average volume (about $8x10^6$ μm^3) of the seeds used for our experiments, although different volumes were also tested.

The crystal seeds used for these calculations had the same aspect ratios of those used for the simulations presented in Section 5.14 of this document.

For TFA-I and TFA-II, the volume at time *t* and concentration *x* was defined considering a cylindrical shape as:

$$V(t,x) = \frac{\pi}{4}\left[L_0 + G_L(x)t\right]\left[W_0 + G_W(x)t\right]^2 \quad \text{(S15)}$$

Where L_0, W_0 are the initial crystal dimensions and $G_L(x)$ and $G_W(x)$ are the average experimental linear growth rates of the corresponding dimensions.

For TFA-IX, the volume at time t and concentration x was calculated from facet distances and their experimental growth rates using the PPC algorithm described in Section 5.9:

$$V(t,x) = f(d_{\{hkl\},0} + G_{\{hkl\}}(x)t) \quad \text{(S16)}$$

Where the initial distances $d_{\{hkl\},0}$ were proportional to the average distances of the seeds measured for our experiments and were scaled to achieve the desired initial volume. Figure S29 shows the calculated growth volumes as a function of solution concentration for four different growth times. Changing the growth volume (and the initial volume, not shown here) has little effect on the relative growth volumes of the TFA polymorphs, and the information given by the different plots is essentially equivalent.

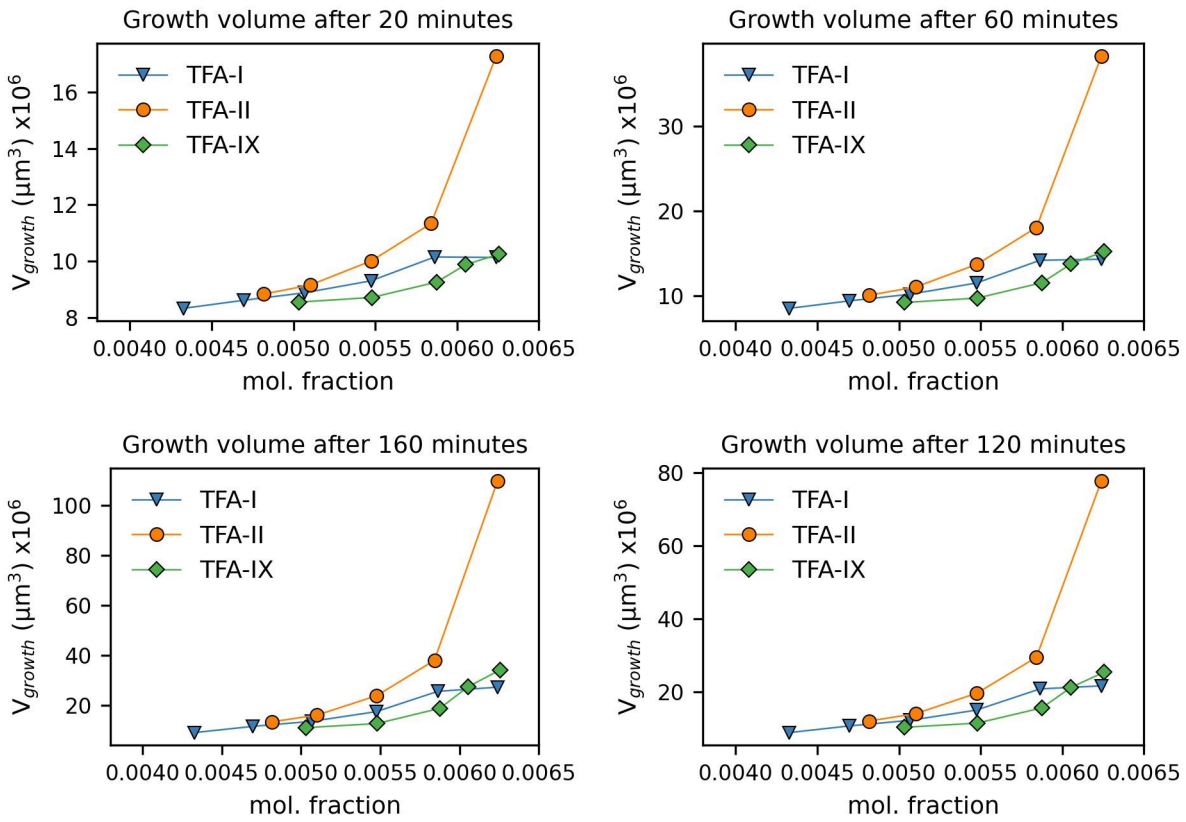

Figure S29. Crystal growth volumes calculated from average linear growth rates for TFA polymorphs for different growth times.

5.12. Calculation of volume growth rates and equivalent diameter growth rates

The same crystal shape approximation used to calculate crystal growth volumes for TFA-I and TFA-II can be used to re-analyse the images collected during our single-crystal growth experiments and to estimate the change in volume as a function of time for each of the measured crystal seeds.

For each image at time *t*, volumes of TFA-I and TFA-II were measured as:

$$V(t) = \frac{\pi}{4} L(t) W(t)^2 \tag{S17}$$

For TFA-IX, the centroid-edge dimensions measured from each image were transformed to facet-specific distances and used to calculate the crystal's volume using the PPC algorithm:

$$V(t) = f(d_{\{hkl\}}(t)) \tag{S18}$$

The diameter of a sphere having equivalent volume as the crystal was then calculated:

$$D(t) = \sqrt[3]{\frac{6V(t)}{\pi}} \tag{S19}$$

Volume growth rates, as well as equivalent diameter growth rates, can then be obtained by linear fitting of the volume vs. time data obtained as described above.

Although the dependence of crystal volume on time is not strictly linear, as it is a function of all growth directions and a cubic dependence on linear dimensions is expected, a linear relationship is used here as approximation. In the case of TFA-I and TFA-II this is justified by the small growth rates of the W and T dimensions compared to the L dimension. For TFA-IX, instead, although the growth rates along different directions have similar magnitude, they are small, and the calculated volume-time dependence deviates only slightly from linearity. Histograms showing the distributions of correlation coefficients R^2 for the volume/diameter vs. time data of our datasets are shown in Figure S30.

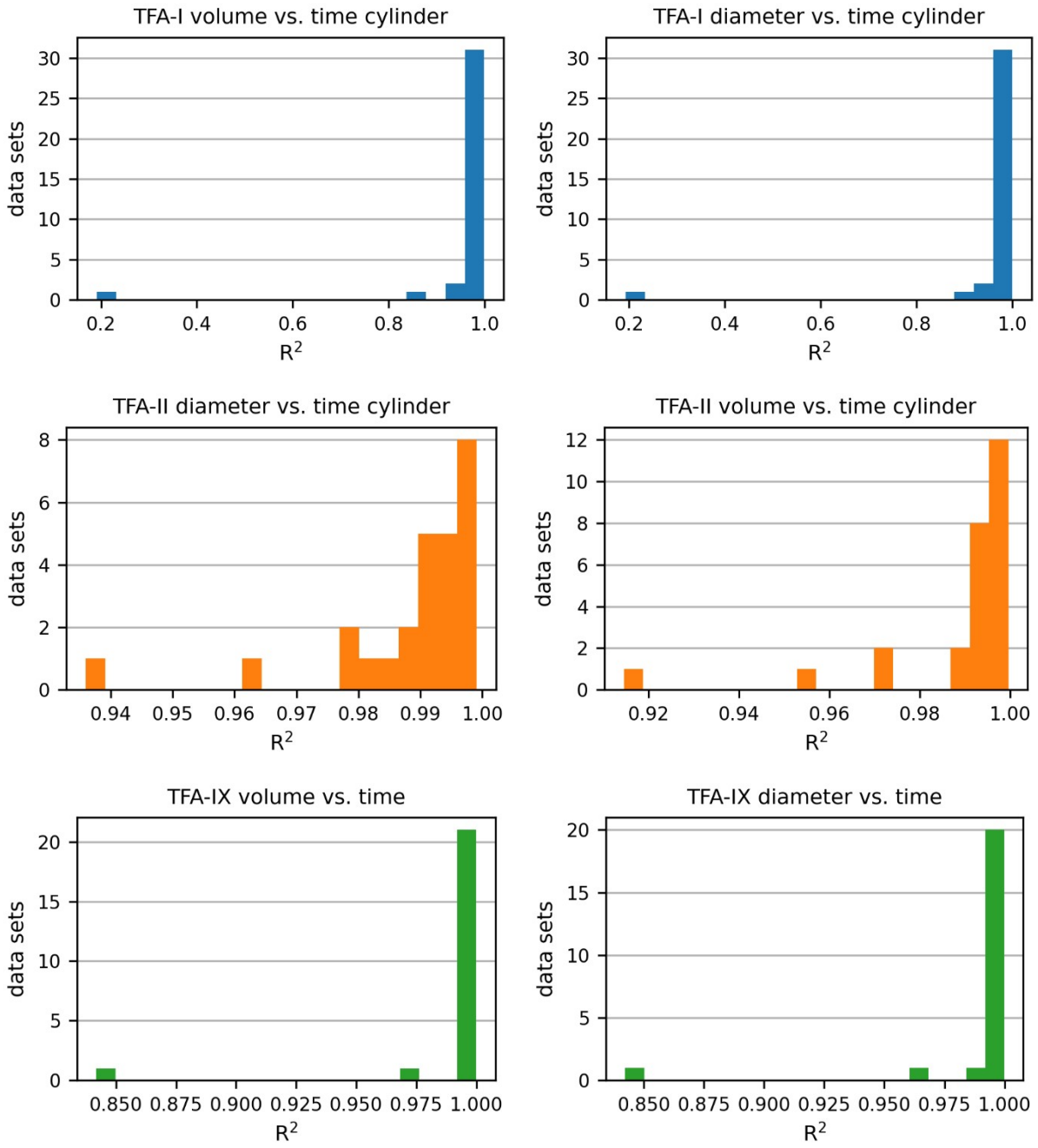

Figure S30. Histograms showing the distributions correlation coefficients of volume/diameter vs. time data for crystals of TFA polymorphs.

The calculated average values for volume and diameter growth rates are reported in Table S9 and shown in Figure S31 as a function of TFA in IPA solution concentration.

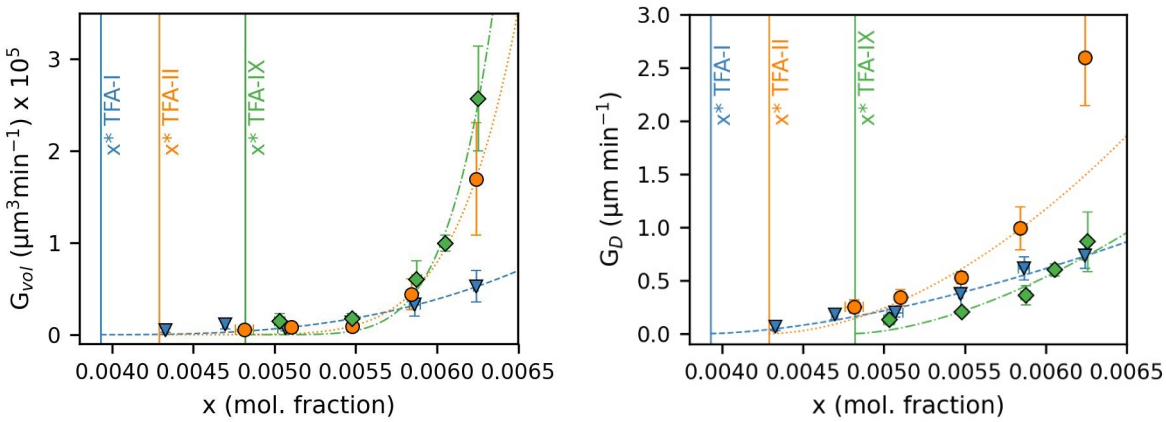

Figure S31. Plots of average volume growth rates (left) and equivalent diameter growth rates (right) for TFA polymorphs as a function of IPA solution concentration. The vertical lines indicate the equilibrium solubility of the polymorphs in IPA at 25 °C. Lines fitting the data were obtained using a power law growth model.

The scenarios described by the calculated volume and equivalent growth rates are quite different. If the volume growth rates are compared, the metastable TFA-IX polymorph appears to grow faster than any of the other two polymorphs. On the other hand, the calculated equivalent diameter growth rates lead to the same conclusion as the calculated growth volumes (see previous section), i.e., that TFA-II always grows faster and that TFA-IX becomes faster than TFA-I at higher solution concentrations. The differences between these two conclusions can be explained by considering the different volumes of the crystal seeds used for our experiments, as well as the change of crystal shape during growth, as described in the next section.

Table S9. Average volume growth rates (G_V) and equivalent diameter growth rates (G_D) calculated for TFA polymorphs.

TFA-I (35 crystals)			
***x* (x10^{-3}) / mol. fraction**	**σ_I**	**G_V (x10^3 µm^3 min^{-1})**	**G_D (µm min^{-1})**
4.33 ± 0.01	0.10	4.8 ± 2.2	0.06 ± 0.03
4.70 ± 0.02	0.20	11.3 ± 50	0.18 ± 0.05
5.07 ± 0.05	0.29	6.7 ± 2.6	0.20 ± 0.04
5.47 ± 0.01	0.39	13.4 ± 9.9	0.37 ± 0.17
5.86 ± 0.04	0.49	32.8 ± 12.9	0.61 ± 0.11
6.24 ± 0.01	0.59	52.6 ± 17.3	0.74 ± 0.13
TFA-II (26 crystals)			
***x* (x10^{-3}) / mol. fraction**	**σ_{II}**	**G_V (x10^3 µm^3 min^{-1})**	**G_D (µm min^{-1})**

4.82 ± 0.06	0.12	5.4 ± 2.8	0.23 ± 0.06
5.10 ± 0.01	0.19	8.2 ± 4.3	0.31 ± 0.07
5.48 ± 0.01	0.28	9.0 ± 1.9	0.53 ± 0.06
5.84 ± 0.03	0.36	44.0 ± 17.0	1.0 ± 0.2
6.24 ± 0.02	0.45	169.7 ± 61.4	2.6 ± 0.5
TFA-IX (23 crystals)			
x **(x10^{-3}) / mol. fraction**	**σ_{IX}**	**G_V (x10^3 µm^3 min^{-1})**	**G_D (µm min^{-1})**
5.03 ± 0.03	0.05	14.9 ± 8.1	0.13 ± 0.05
5.48 ± 0.02	0.14	17.7 ± 4.3	0.20 ± 0.02
5.88 ± 0.03	0.22	59.9 ± 20.2	0.36 ± 0.09
6.05 ± 0.02	0.26	99.7 ± 8.9	0.60 ± 0.06
6.25 ± 0.02	0.30	257.0 ± 57.1	0.9 ± 0.3

Table S10. Parameters obtained by fitting a power law expression to equivalent diameter growth rates of TFA-I, TFA-II and TFA-IX calculated from single-crystal measurements.

Form	**k_1 (µm min^{-1})**	**g**	**SSR**
TFA-I	1.7 ± 0.4	1.6 ± 0.2	0.009
TFA-II	6.2 ± 5.0	1.8 ± 0.6	1.25
TFA-IX	5.3 ± 3.0	1.6 ± 0.3	0.03

5.13. Effect of different shape approximations on growth rates of TFA-I and TFA-II

As introduced in Section 5.2, the 3D shape of needle crystals of TFA-I and TFA-II can be approximated with either a cylindrical shape, as we have done here, or with a parallelepipedal box of dimensions L, W and T. The latter approximation requires an assumption about the thickness of the box, which ideally should be measured experimentally. We have tried analysing our data using this box approximation and assuming several T/W ratios between 0.4 and 1.0. The lower limit of 0.4 was chosen by comparison with the experimental morphology of TFA-I, which had a T/W ratio of 0.46. Figure S32 shows the growth rates of the equivalent diameter of the TFA polymorphs depending on the chosen T/W ratio, where the solid lines were obtained by fitting a power law equation using the parameters shown in Table S11. The black dotted and dash-dotted lines in the figure represent power law growth rates for a cylindrical shape (using parameters of Table S10).

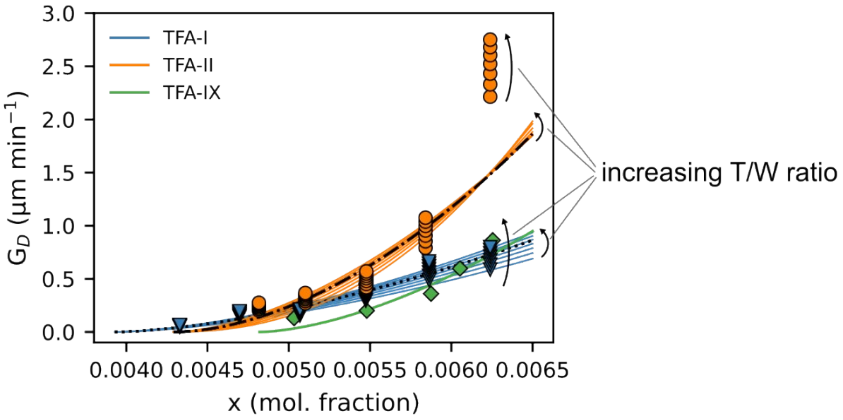

Figure S32. Effect on the estimated equivalent diameter growth rates of TFA-I and TFA-II of changing the T/W ratio of the box used to approximate their shape. Solid lines are modelled using a power law equation and the parameters of Table S11. The dotted and dash-dotted lines were obtained with the parameters of Table S10 for TFA-I and TFA-II, respectively.

Table S11. Growth parameters for a power law equation for the equivalent diameter growth rates of TFA-I and TFA-II obtained using box shape approximations with variable T/W ratios.

TFA-I		
T/W ratio	**k_1 (µm min^{-1})**	**g**
0.4	1.36 ± 0.28	1.6 ± 0.2
0.5	1.46 ± 0.30	1.6 ± 0.2
0.6	1.55 ± 0.32	1.6 ± 0.2
0.7	1.63 ± 0.34	1.6 ± 0.2
0.8	1.71 ± 0.36	1.6 ± 0.2
0.9	1.78 ± 0.37	1.6 ± 0.2
1.0	1.84 ± 0.38	1.6 ± 0.2
TFA-II		
T/W ratio	**k_1 (µm min^{-1})**	**g**
0.4	8.9 ± 7.8	2.3 ± 0.7
0.5	8.0 ± 6.9	2.1 ± 0.7
0.6	7.2 ± 6.0	2.0 ± 0.7
0.7	6.5 ± 5.4	1.9 ± 0.6
0.8	6.1 ± 4.9	1.8 ± 0.6
0.9	5.8 ± 4.6	1.7 ± 0.6
1.0	5.6 ± 4.3	1.7 ± 0.6

We note that changing the T/W ratio used for the box shape approximation has some effect on the absolute values of the estimated equivalent diameter growth rates, but that the relative growth rates of the three TFA polymorphs with respect to solution concentration remain unchanged. Notably, the

concentration at which TFA-IX becomes faster than TFA-I increases as the T/W ratio of the box used to describe TFA-I increases, as shown in Table S12, where intersection values were calculated based on the power law model predictions of Figure S32.

Table S12. IPA solution concentration where TFA-IX is faster than TFA-I as a function of the T/W ratio of the box chosen to describe TFA-I crystals.

T/W ratio of TFA-I	Concentration (mol. fraction)
0.4	0.0059
0.5	0.0060
0.6	0.0061
0.7	0.0061
0.8	0.0062
0.9	0.0064
1	0.0065

5.14. Effect of crystal size and shape on calculated volume growth rates and diameter growth rates

Table S12 shows the average dimensions of the single-crystal seeds used for our experiments. Compared to the very thin needles measured for TFA-I and TFA-II, the blocky crystals of TFA-IX are much larger, with volumes that are at least one order of magnitude larger. In addition, crystals of TFA-IX have an equant shape and grow with similar rates in all directions. Crystals of TFA-I and TFA-II, on the other hand, are very elongated and their growth along the needle axis is two orders of magnitude faster than along the remaining directions. Thus, while the shape of TFA-IX crystals is expected to show little variations during growth, the shapes of TFA-I and TFA-II crystals change constantly. For this reason, the use of an equivalent diameter to describe the growth rate of these needle crystals might not be appropriate. The equivalent diameter, however, provides a useful single characteristic length to compare the growth rates of the different polymorphs.

The effect of different initial crystal seed volumes (and of different initial aspect ratios for TFA-I and TFA-II) on the calculated volume growth rates and equivalent diameter growth rates were estimated by simulating the growth of TFA crystals for 120 minutes using the average experimental linear growth rates. Linear growth rates were assumed constant and size-independent. For each time interval Δt (typically 1 minute), volumes were calculated as described in Section 5.11 of the present document. The simulated crystal volumes (and equivalent-diameter) vs. time data were then linearly fitted to extract values of G_{vol} and G_D as a function of the different seed sizes.

Calculations were performed for seed volumes between $9x10^4$ and $2x10^7$ μm^3 and for three IPA concentrations at which the growth rates of all three polymorphs had been measured (x = 0.0055, 0.0059, 0.0063).

Figures S33, S34, and S35 show the calculated relative change of crystal aspect ratio, the volume growth rate and the equivalent diameter as a function of crystal volume for TFA-I, TFA-II and TFA-IX, respectively.

Table S12. Average length (L), width (W), aspect ratio (AR), volume (V) and surface area (A) of the TFA seeds used for the single-crystal growth rate experiments presented in this work. The volumes were calculated as described in the sections above. N is the number of crystal seeds measured for each polymorph.

	N	**L (µm)**	**W (µm)**	**AR[a]**	**V (μm^3)**	**A (μm^2)**
TFA-I	35	559	64	8.7	$2.3 x10^6$	$1.3 x 10^5$
TFA-II	26	348	46	7.6	$8.1 x10^5$	$6.2 x 10^4$
TFA-IX	23	582	356	1.9 / 2.7	$1.6 x10^7$	$4.0 x 10^5$
[a] L/W for TFA-I and TFA-II; L_1/L_3 and L_2/L_3 for TFA-IX (see Figure S35)						

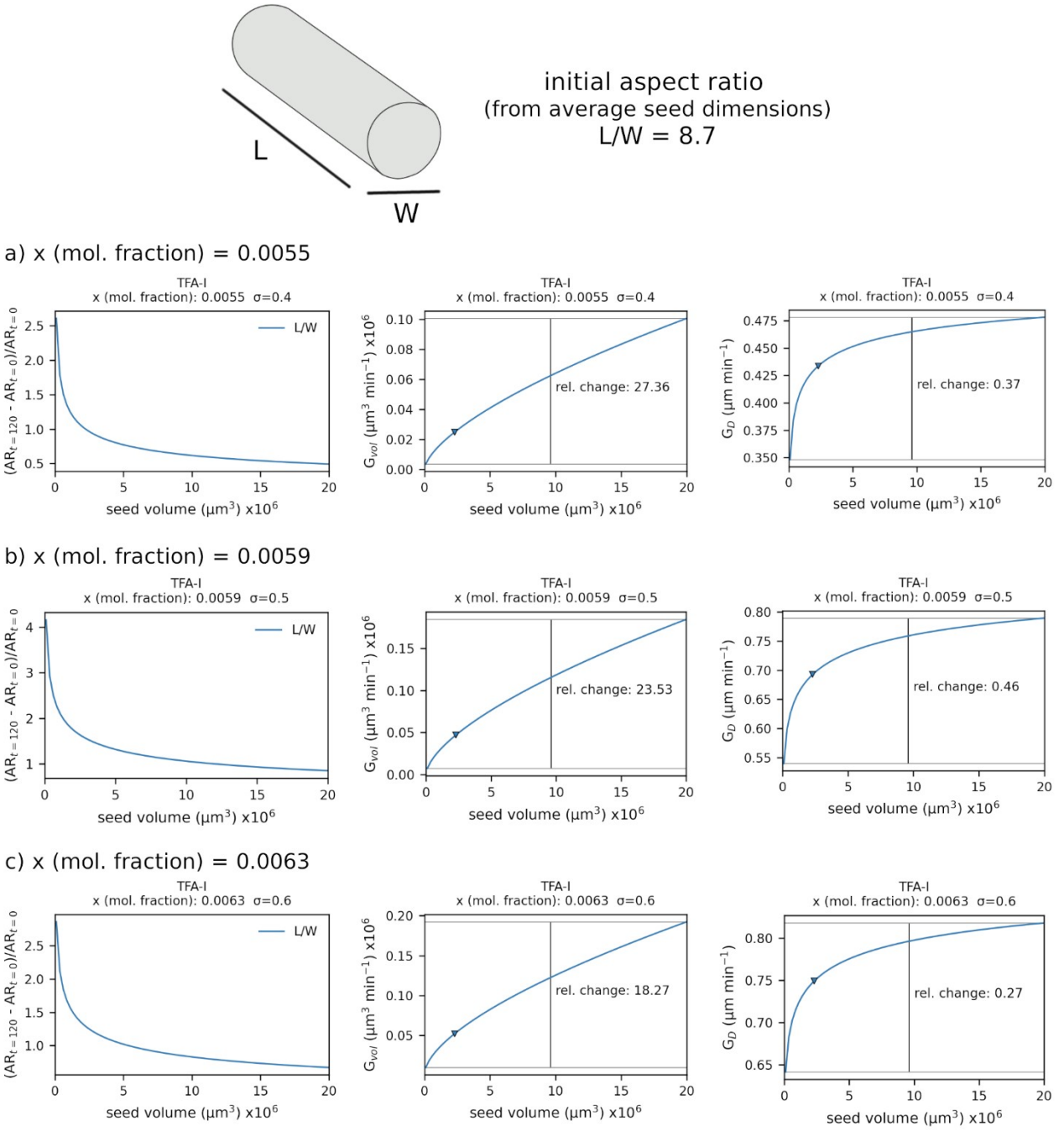

Figure S33. The effect of different initial seed volumes on calculated growth rates for TFA-I for three different IPA solution concentrations. The quantities presented here were calculated assuming constant linear growth rates. The average linear growth rates from experiments were used (see text). Relative change in aspect ratio after 120 minutes (left column); change of the calculated volume growth rate, G_V (middle column); change of the calculated equivalent diameter growth rate, G_D (right column). At the top: the shape used for TFA-I for these calculations, based on the average seed dimensions of TFA-I. The thickness T was calculated from W and is not shown here. The triangle marker in the plots indicates the average volume of TFA-I seeds used in the experiments.

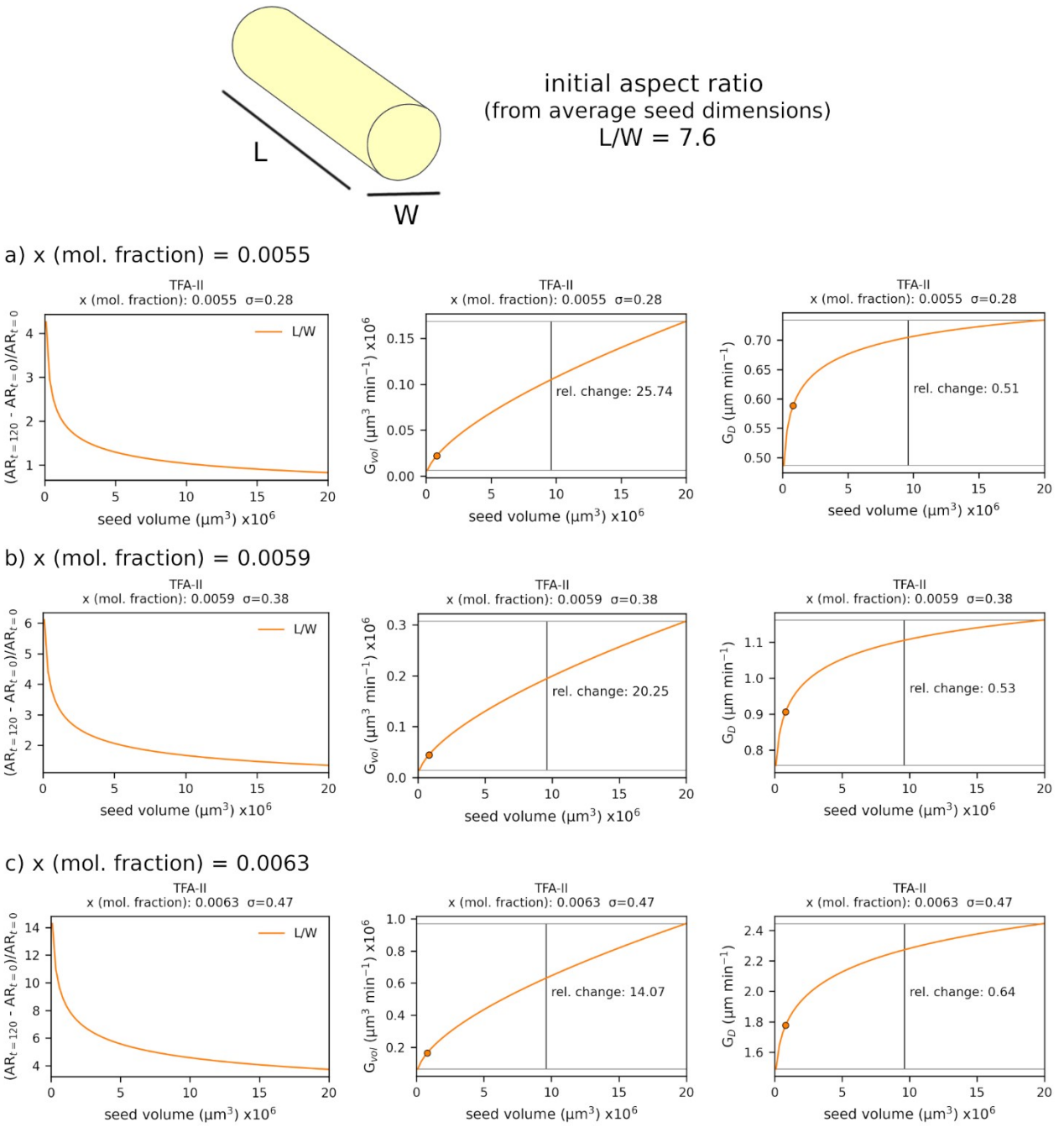

Figure S34. The effect of different initial seed volumes on calculated growth rates for TFA-II for three different IPA solution concentrations. The quantities presented here were calculated assuming constant linear growth rates. The average linear growth rates from experiments were used (see text). Relative change in aspect ratio after 120 minutes (left column); change of the calculated volume growth rate, G_V (middle column); change of the calculated equivalent diameter growth rate, G_D (right column). At the top: the shape used for TFA-II for these calculations, based on the average seed dimensions of TFA-II. The thickness T was calculated from W and is not shown here. The circle marker in the plots indicates the average volume of TFA-II seeds used in the experiments.

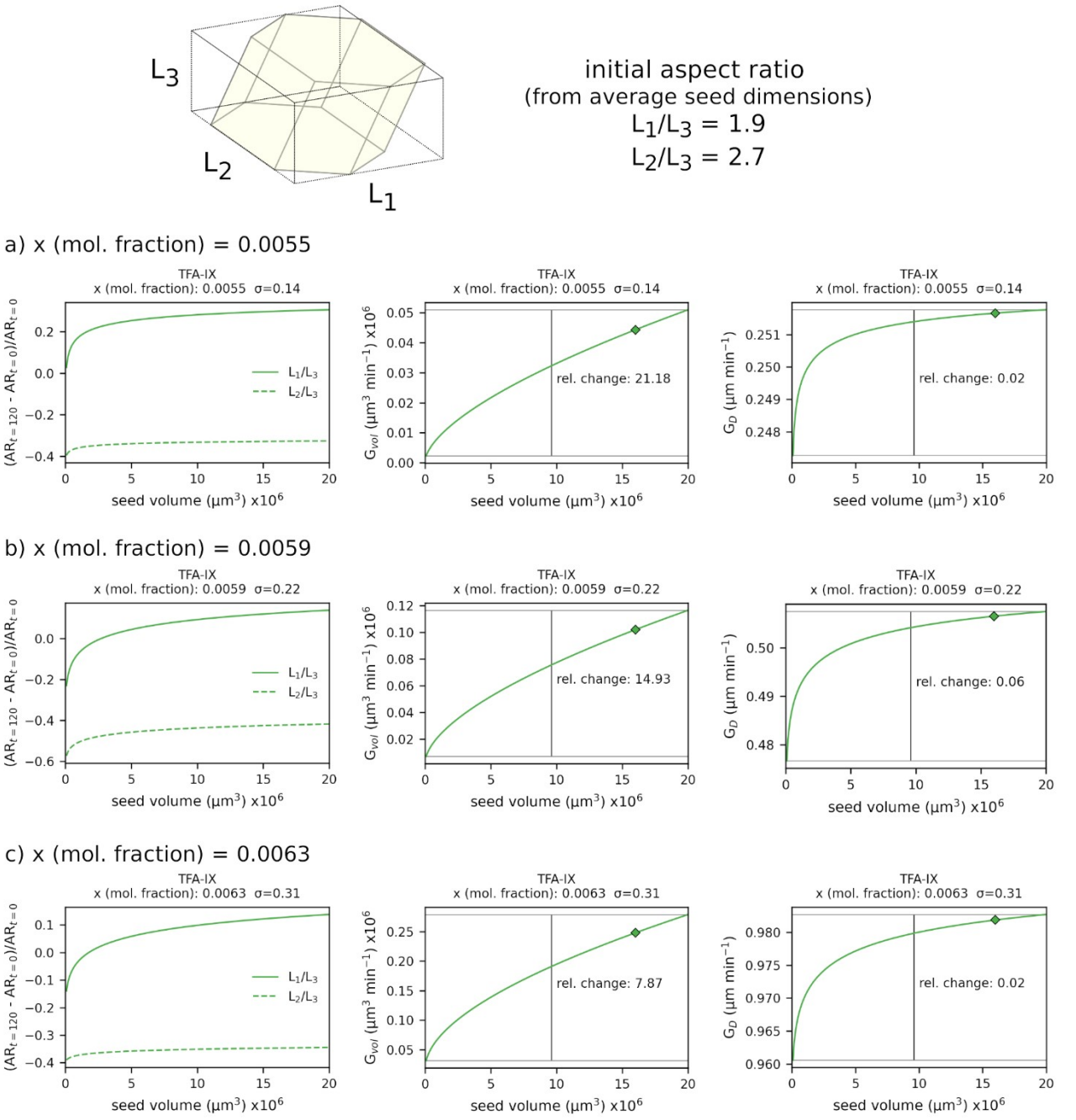

Figure S35. The effect of different initial seed volumes on calculated growth rates for TFA-IX for three different IPA solution concentrations. The quantities presented here were calculated assuming constant linear growth rates. The average linear growth rates from experiments were used (see text). Relative change in aspect ratio after 120 minutes (left column); change of the calculated volume growth rate, G_V (middle column); change of the calculated equivalent diameter growth rate, G_D (right column). At the top: the shape of TFA-IX used for these calculations, calculated from the average dimensions of seeds of TFA-IX. The diamond marker in the plots indicates the average volume of TFA-IX seeds used in the experiments.

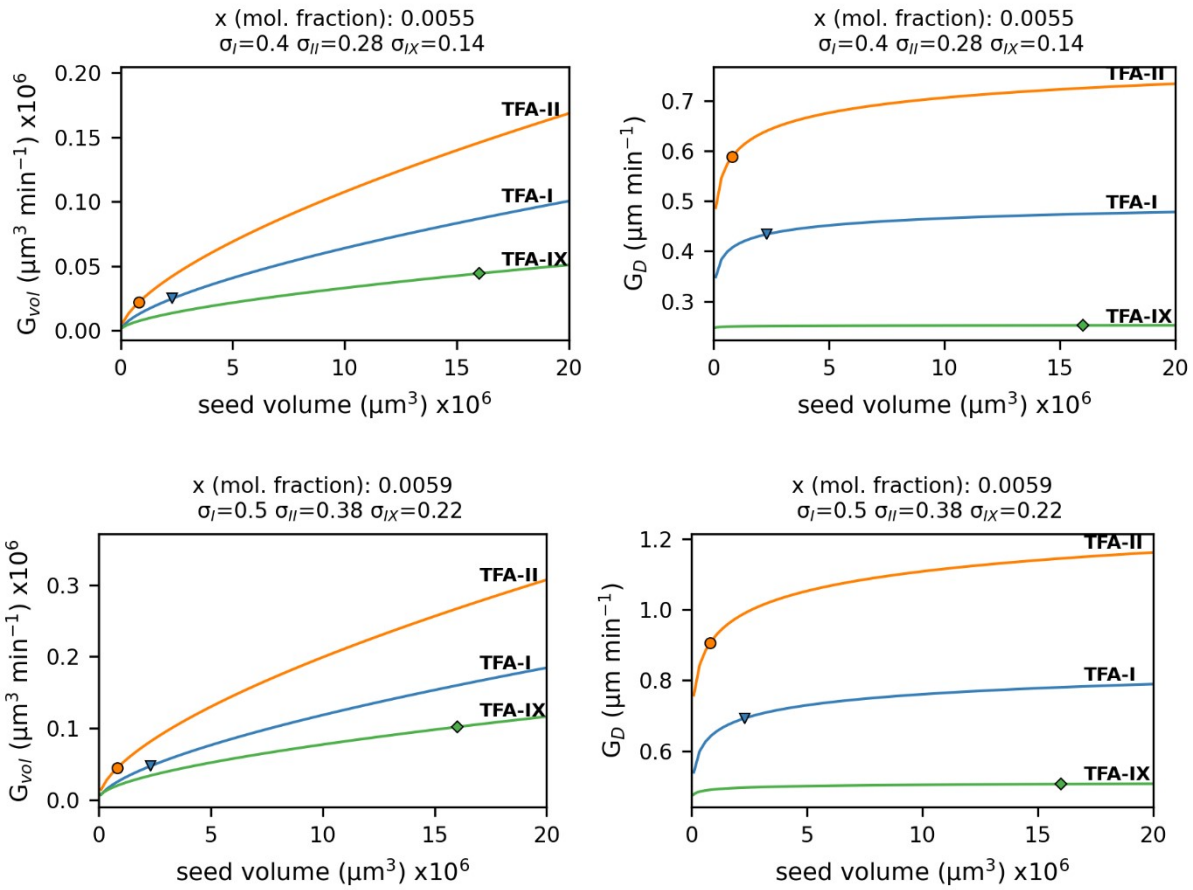

Figure S36. Effect of different seed volumes on calculated volume growth rates (G_{vol}, left) and equivalent diameter growth rates (G_D, right).

When the volume of the crystal seeds is small, the shape of the needle crystals of TFA-I and TFA-II changes drastically, although this effect diminishes as the seeds become larger (i.e., as the change in dimension with time is small compared to the dimension itself and the crystal shape doesn't change as drastically as for smaller seeds). As a result, the calculated volume growth rates vary by about 3000% and the diameter growth rates vary by about 50% between seed volumes of $9x10^4$ and $2x10^7$ μm^3 considered here. For TFA-IX, on the other hand, the shape of the crystals shows a much smaller variation, and although the change in calculated volume growth rate is still as high as 2000%, the calculated equivalent diameter growth rates vary only slightly for different seed volumes.

The equivalent diameter growth rates seem to tend to a plateau for large enough seed volumes. Thus, according to our analysis, equivalent diameter growth rates of crystals with very different shapes should be ideally compared only for large enough crystal volumes, i.e, when they show little change with changing crystal volume/shape. In alternative, growth rates measured for seeds of identical volume should be compared. Practically, however, the size of the seed crystals used for measurements

of growth rates of single-crystals can be variable, and the seeds dimension can be affected by dissolution and/or cutting of the crystals to prepare them for the measurement.

Comparison of crystal volume growth rates should instead be carried out only for measured seeds having the same volume. In our case, the seed crystals of TFA-IX have too different volumes compared to TFA-I and TFA-II, and the volume growth rates should not be used to determine which polymorph grows faster.

6. Seeded isothermal desupersaturation (SID) batch experiments

Growth kinetics of TFA-I and TFA-II in IPA at 25 °C were also measured via seeded isothermal desupersaturation (SID) experiments in a 75 ml reactor. Solution concentration was monitored using an ATR-UV probe.[42,43]

Experiments for TFA-IX were unsuccessful, as this polymorph promptly transformed to either TFA-I or TFA-II during measurements. It is possible that the seeds of TFA-IX used for these experiments contained impurities of TFA-I, as these two polymorphs can crystallise together. Figure S37 shows needle crystals of TFA-I which formed on top of crystals of TFA-IX.

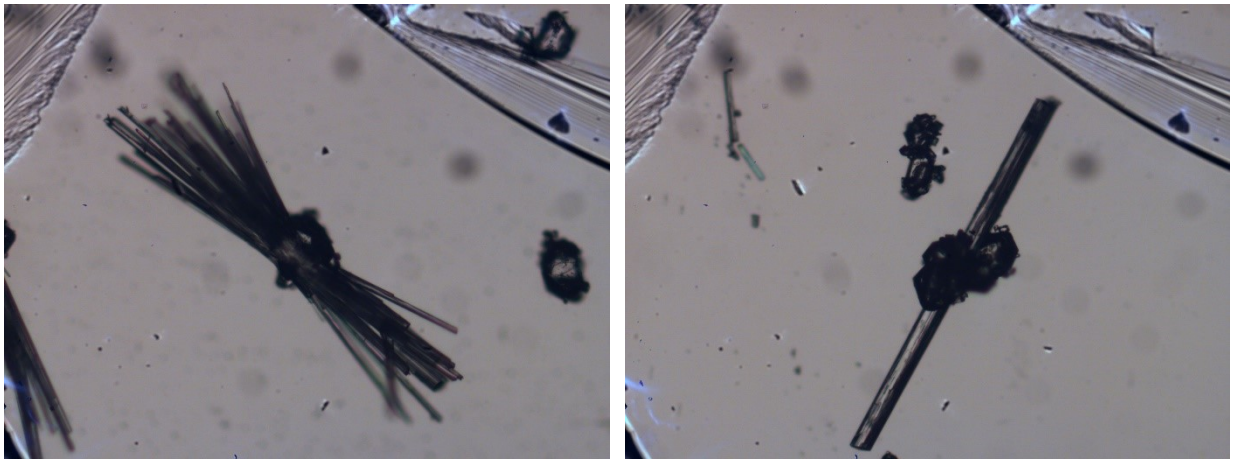

Figure S37. Needle crystals of TFA-I formed on crystal seeds of TFA-IX during SID experiments.

6.1. UV Calibration and data processing

Data from UV measurements were analysed using a two-component partial least squares (PLS) regression model.[44] The PLS model was parametrised using UV spectra collected for solutions of TFA in IPA of known concentration at various temperatures (18 - 45 °C). Because SID experiments were performed over a relatively long period of time (three months), new calibration data were

collected periodically to account for factors like loss of intensity of the UV lamp and unwanted bending of the fibre optics cable connecting the probe to the UV spectrometer.

The UV spectra of TFA present three evident absorption peaks around 210, 290 and 350 nm (Figure S38). Only the latter two peaks were used for our analysis, as the peak at 210 nm was close to the wavelength range limit of our UV instrument. Collected UV spectra were pre-processed applying a single-point baseline correction at 420 nm. Figure S39 shows the correlation of measured and predicted concentrations for a typical calibration model. We note that using two components for our PLS model was probably unnecessary, and that a model with a single component (or measuring the concentration using the Lambert-Beer law) would have likely sufficed.

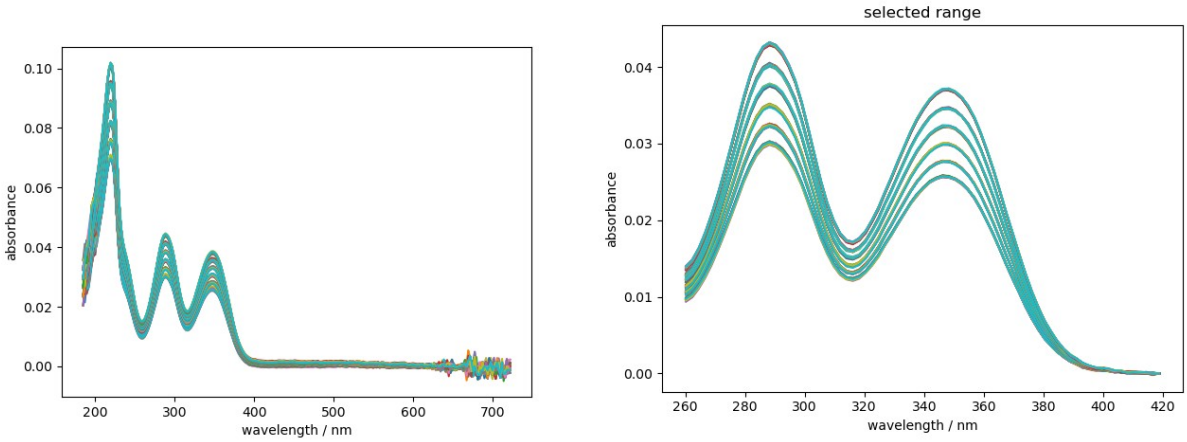

Figure S38. (Left) UV spectra of solutions of TFA in IPA collected during SID experiments. (Right) the region of the UV spectra between 260-420 nm which was used for both calibration and analysis of data collected during SID experiments.

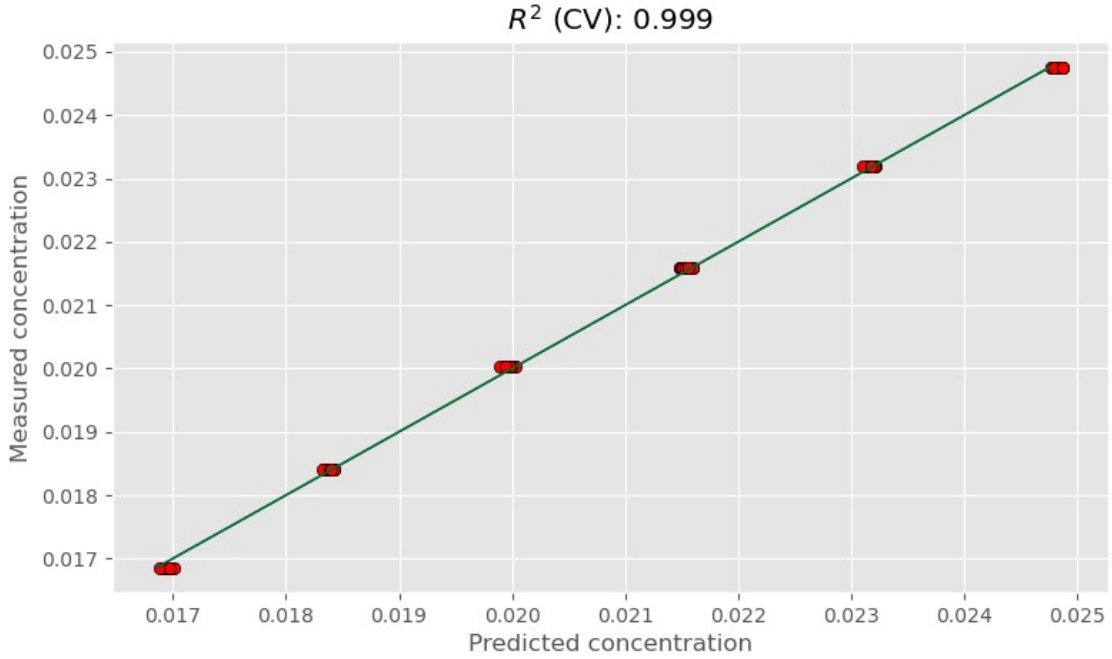

Figure S39. Cross validation plot showing the correlation between measured and predicted concentration of TFA solutions in IPA from calibration.

6.2. Population Balance Modelling (PBM)

The growth rate parameters for the TFA-I and TFA-II crystal population were fitted using a 1-Dimensional population balance model coupled with a concentration equation, to represent the solid and liquid phases, respectively. The population balance equation used, assumes a well-mixed batch crystallizer where no breakage or agglomeration takes place:

$$\frac{\partial f(t,x)}{\partial t} + G\frac{\partial f(t,x)}{\partial x} = 0 \tag{S20}$$

$$f(x, t = 0) = f_0(x) \tag{S21}$$

where f is the distribution function, t is time, G is the size-independent growth rate and x is the crystal size. The initial condition of the distribution function is equal to the seeds, f_0. The LHS is equated to zero since we assumed no primary nucleation takes place because of the addition of seeds and secondary nucleation is assumed insignificant due to relatively low stirring rate. The size-independent growth rate is given by:

$$G = k_1(S - 1)^g \tag{S22}$$

where k_1 and g are parameters to be fitted. The supersaturation S is defined as:

$$S = \frac{c}{c^*(T)} \tag{S23}$$

$$c(t=0) = c_0 \tag{S24}$$

where, $c^*$is the solubility, T is the temperature, c is the concentration of the solution and c_0 is the initial concentration.

The PBM was coupled with the equation of the following concentration profile:

$$\frac{dC}{dt} = -k_V \rho \frac{d\mu_3}{dt} \tag{S25}$$

where C is the concentration, ρ is the density of the crystal and μ_3 is the third central moment of the distribution. The shape factor k_v was equal to $\frac{1}{6}\pi$, since the needles of TFA-I and TFA-II were simplified with spheres and the characteristic length corresponded to the sphere diameter.

The moments, μ_i, of the distribution function are given by:

$$\mu_i = \int_0^\infty x^i f(t,x)dx, \qquad i = 0, 1, 2, \ldots,$$

The solution of the PBM was given by the upwind flux scheme of the finite volume method.[45,46]

The 2-Dimensional size distribution was measured using the imaging device described by Neoptolemou et al.[47] and was further simplified to a 1-Dimensional size distribution. For volume conservation, the particles were represented by a cylinder and a sphere for the 2D and 1D distributions, respectively.

The k_1 and g parameters were fitted by minimizing the squared difference of the simulation and experimental concentrations. The following function was minimized:

$$\Phi(k_1, g) = \frac{1}{N_E}\sum_{i=1}^{N_E}\frac{1}{N_P}\sum_{j=1}^{N_P}(y_{ij} - \hat{y}_{ij}(k_1, g))^2 \tag{S26}$$

where N_E is the number of experiments of one of the two polymorphs, N_P is the number of points in time of the concentration profile, y_{ij} and $\hat{y}_{ij}$ are the experimental and simulated concentrations of experiment i at point j. The covariance matrix was used to calculate the standard errors.

6.3. Seeds and SID experiments

Population size distributions of crystals of TFA-I and TFA-II before (Figures S40 and S41) and after SID experiments were produced using the methodology described in Neoptolemou et al.[47] The

average crystal length and width, as well as the volume of the corresponding cylindrical shape used to describe the crystals are presented in Table S13.

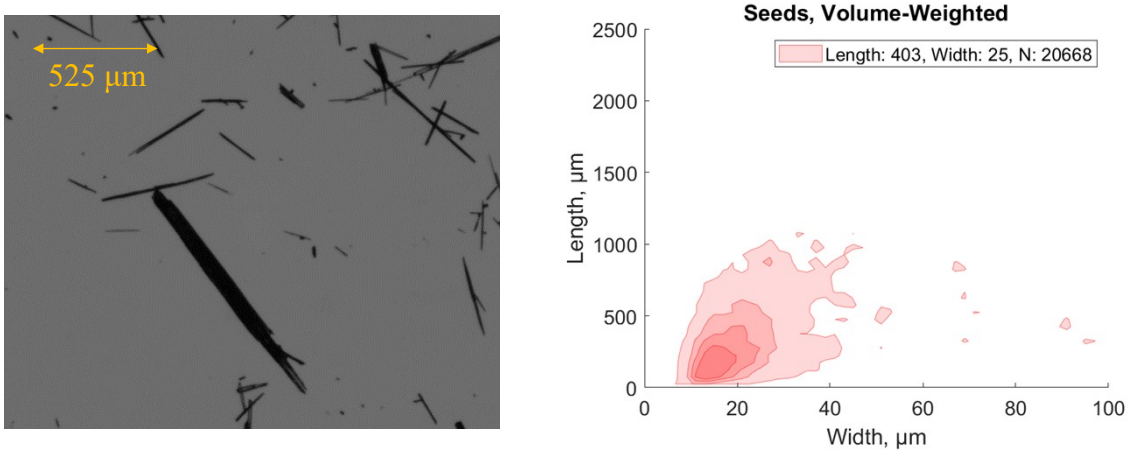

Figure S40. Crystal seeds used for desupersaturation experiments of TFA-I. Left: Grayscale microscope image. Right: Volume-weighted particle size and shape distribution. N is the number of particles characterized.

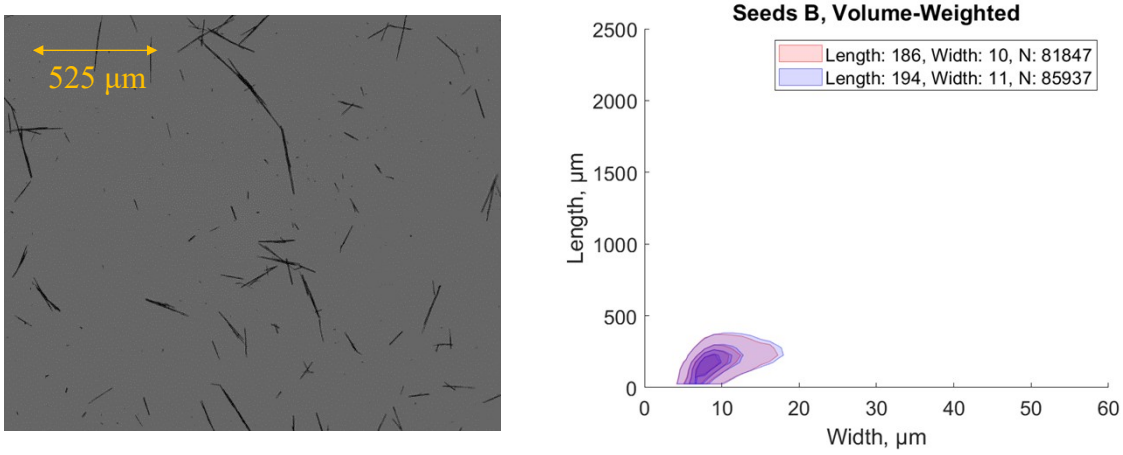

Figure S41. Crystal seeds used desupersaturation experiments of TFA-II. Left: Grayscale microscope image. Right: Volume-weighted particle size and shape distribution. N is the number of particles characterized.

Table S13. PSSDs of TFA-I and TFA-II from the SID experiments.

TFA-I[a]							
Experiment	**x / mol fract.**	**S_I**	**L (µm)**	**W (µm)**	**V (µm³)**	**relative L change[b]**	**relative W change[b]**
seeds	-	-	403	25	2.0E+05	-	-
1	0.0055	1.41	520	37	5.6E+05	0.3	0.5
2	0.0054	1.37	657	39	7.8E+05	0.6	0.6
3	0.0055	1.41	582	36	5.9E+05	0.4	0.4
4	0.0051	1.31	426	31	3.2E+05	0.1	0.2
5	0.0047	1.20	722	36	7.3E+05	0.8	0.4
6	0.0050	1.29	529	35	5.1E+05	0.3	0.4

TFA-II							
Experiment	**x / mol fract.**	**S_{II}**	**L / µm**	**W / µm**	**V (µm³)**	**relative L change**	**relative W change**
seeds	-	-	190	11	1.8E+04	-	-
1	0.0056	1.28	440	20	1.4E+05	1.32	0.80
2	0.0055	1.28	399	19	1.1E+05	1.10	0.73
3	0.0051	1.17	432	15	7.6E+04	1.27	0.36
4	0.0053	1.24	548	22	2.1E+05	1.88	1.00
5	0.0053	1.24	393	21	1.4E+05	1.07	0.91
6	0.0047	1.09	331	14	5.1E+04	0.74	0.27
7	0.0050	1.16	538	24	2.4E+05	1.83	1.18

[a]volume weigthed average from measurements; [b] change of measured dimension relative to the seeds

6.4. Results

Figure S42 shows the growth rate curves for the characteristic length of TFA-I and TFA-II in IPA at 25 °C. The curves were calculated with a power law model using the parameters presented in Table S14. Figures S43 and S44 show the concentration curves as measured from our experiments, as well as concentrations simulated by our PBM model.

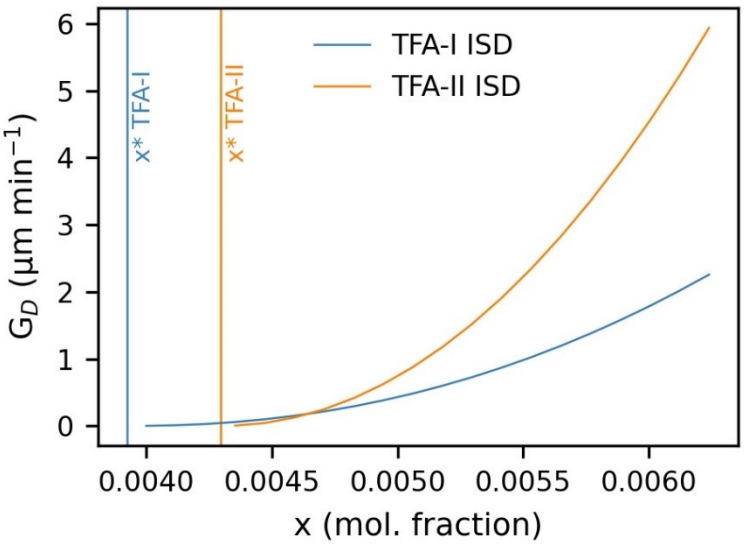

Figure S42. Growth rates of the characteristic dimension (equivalent diameter) of TFA-I and TFA-II in IPA at 25 °C obtained from SID experiments. The curves were calculated using a power law expression and the parameters presented in Table S13

Table S14. Fitted growth rate parameters for TFA-I and TFA-II from SID experiments in IPA.

Form	k_1 (µm min^{-1})	g	SSR
TFA-I	7.1 ± 0.1	2.16 ± 0.01	0.0062
TFA-II	30.2 ± 0.7	2.06 ± 0.01	0.0013

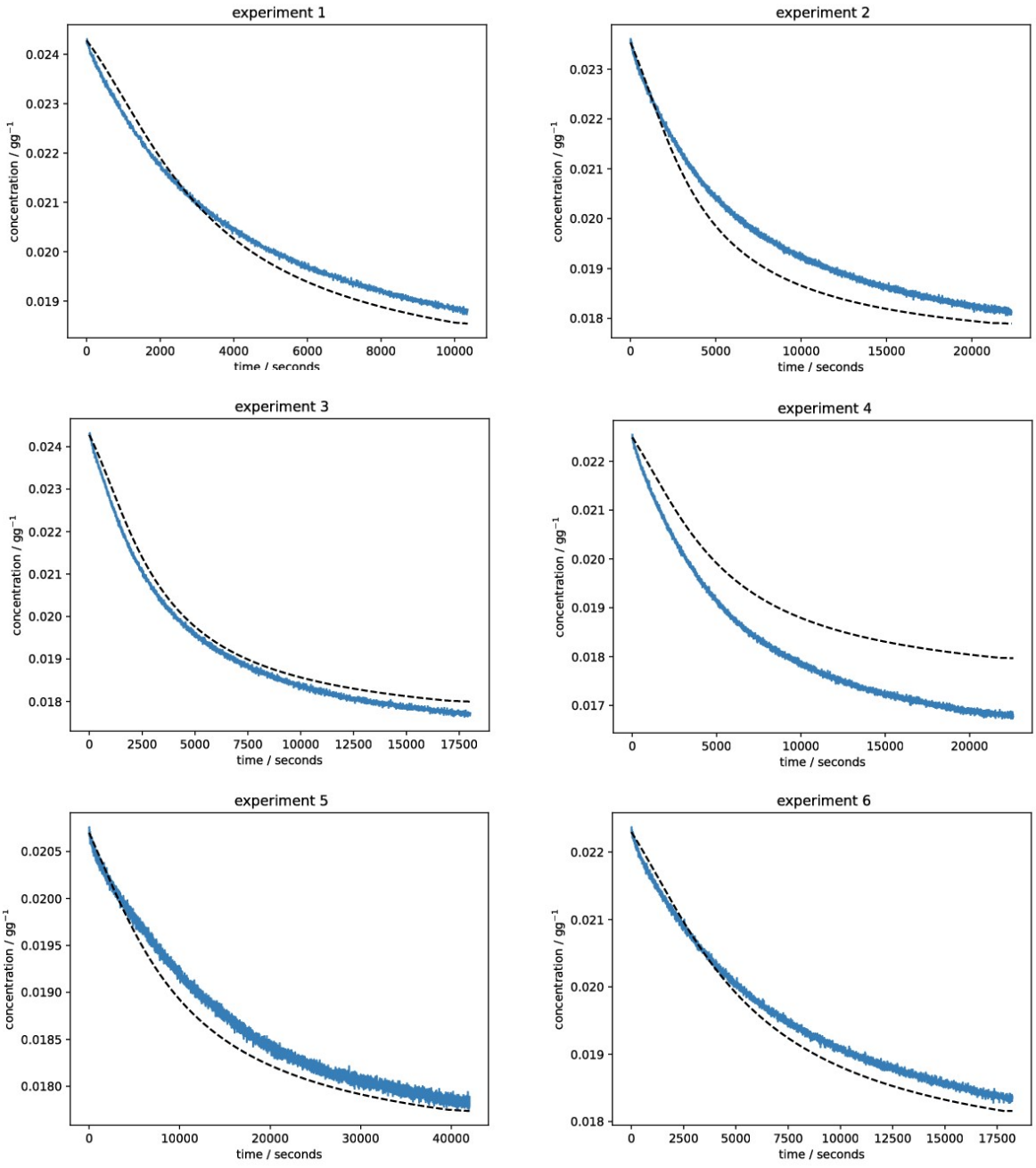

Figure S43. Experimental (blue) and simulated (black dashed) concentration profiles of desupersaturation of TFA I.

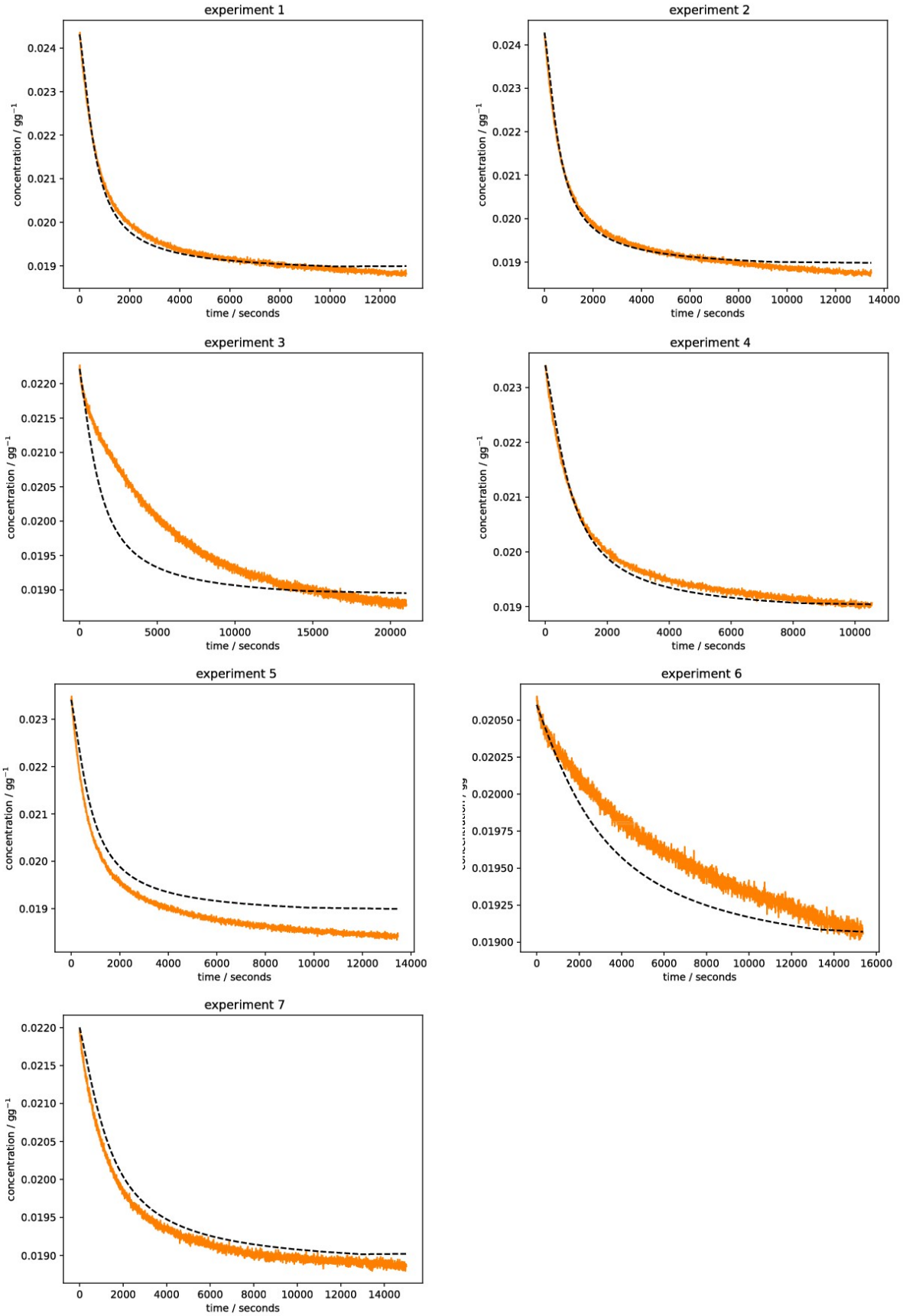

Figure S44. Experimental (orange) and simulated (black dashed) concentration profiles of desupersaturation of TFA II.

7. Analysis of errors and error propagation in measurements of single-crystal growth rates

In this section, we analyse the possible sources of errors in our measurements of growing single-crystals and how these errors are carried on in the calculation of growth rates and averaged quantities.

7.1. Sources of systematic error

All measurements of single-crystal dimensions presented in this work were performed using automated MATLAB image processing algorithms written in our group. Although the codes used to measure either the needle crystals of TFA-I and TFA-II or the blocky crystals of TFA-IX work in inherent different ways, they both rely on image pre-processing, namely conversion to grayscale and image binarization. The latter step, in particular, is essential to determine the boundaries of the object that will be measured. The identification of the correct boundary will in turn depend on the level of blurring of the crystal edges in the original image.

To quantify the error due to the boundary recognition, we collected multiple images of TFA crystals at different levels of focus and rotated at different orientations. We then repeatedly measured relevant distances from the collected images, and we calculated the average standard deviation as the square root of the sum of the variances of each set of distances. We found this average standard deviation on the measured length *l'*, $\sigma_{l'}$, to be 3 μm.

Another source of error in our measurements is due to the fact that the cuvette containing the crystal seed does not lie flat in the growth cell, but at an angle which is the result of the different thicknesses of the cuvette at its bottom and at the neck opening. This will result in the measured object being slightly tilted with respect to the image plane, and in a distortion of the actual measured distance which is proportional to:

$$l = \frac{l'}{cos\psi} \tag{S27}$$

Where *l* and *l'* are the *real* and the measured lengths, respectively, and ψ is the angle between the cuvette containing the crystal seed and the bottom of the growth cell. The error on the real length, σ_l, will also be proportional to the error on the measured length, $\sigma_{l'}$, according to eq. S27. Figure S45 shows the influence of the cuvette angle ψ on the error of the real length. It can be seen from the figure that this error is very small for small cuvette angles (1% additional error for an angle of 10°). In our case, we measured the inclination of our cuvettes to be of about 3°. This small cuvette angle results in a small overall error that we decided nonetheless to include in our measured data. Therefore,

each linear dimension directly measured from the collected images has an associated systematic error σ_l of about 3 μm, which is propagated in all of the derived quantities.

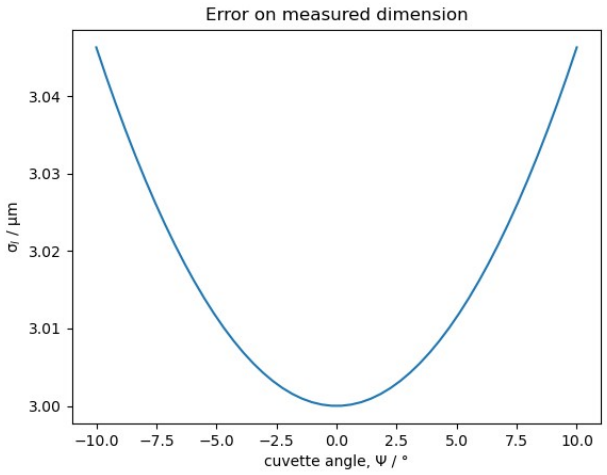

Figure S45. Effect of the tilt angle of the cuvette used for the measurements of single-crystal growth rates on the error on the measured dimensions, σ_l.

7.2. Error propagation

The systematic errors presented above were propagated in derived quantities according to the theory of error propagation:

$$\sigma_f = \sqrt{\sum_i \left(\frac{\delta f}{\delta x_i}\sigma_{x_i}\right)^2} \tag{S28}$$

Where f is a function of the variables x_i.

7.3. Linear fitting of dimension vs. time data: error on the calculated slopes

The single-crystal growth rates presented in this work were calculated by linear fitting of the measured crystal dimensions against time:

$$y = Gx + c \tag{S29}$$

Where y is our measured quantity, G is the rate calculated as the slope of the best-fit curve and c is the intercept.

The best-fit slope can also be expressed as:[48]

$$G = \frac{n\sum_{i}^{n} x_i y_i - \sum_{i}^{n} x_i \sum_{i}^{n} y_i}{n\sum_{i}^{n} x_i^2 - \left(\sum_{i}^{n} x_i\right)^2} \quad \text{(S30)}$$

When each y_i measurement has the same error σ, and if the error on x is considered negligible (in our case the interval between x values, the time data, is controlled by the image collection software) then the standard deviation of the slope can be calculated as the square root of its variance, which is calculated from eq. S30 considering error propagation:

$$\sigma_G^2 = \frac{n\sigma^2}{n\sum_{i}^{n} x_i^2 - \left(\sum_{i}^{n} x_i\right)^2} \quad \text{(S31)}$$

If each y_i measurement, instead, has a different error σ_i, then the variance of the slope is:

$$\sigma_G^2 = \frac{1}{D}\sum_{i}^{n} \frac{1}{\sigma_i^2} \quad \text{(S32)}$$

Where:

$$D = \sum_{i}^{n} \frac{1}{\sigma_i} \sum_{i}^{n} \frac{x_i}{\sigma_i} - \left(\sum_{i}^{n} \frac{x_i}{\sigma_i}\right)^2 \quad \text{(S33)}$$

For TFA-I and TFA-II, the error on linear growth rates were calculated using eq. S31, while the errors on the derived quantities (i.e., volume growth rates) were calculated using eq. S32.

7.4. Error on the volume of TFA-IX crystals

Contrary to TFA-I and TFA-II crystals, whose volume was calculated using either eq. S15 (Section 5.11) or equation S21 (Section 5.12), the volume of TFA-IX crystals was calculated using the PPC algorithm presented in Section 5.9. As a consequence, the propagation of error from experimental measurements could not be directly calculated. Instead, the error on TFA-IX volumes was determined by calculating upper and lower volume limits defined by the experimental errors of the defining facet distances:

$$V_{upper/lower} = f(d_{hkl} \pm \sigma_{d_{hkl}}) \quad \text{(S34)}$$

The error on the volume was then calculated as:

$$\sigma_V = \frac{[(V(d_{hkl}) - V_{lower}) + (V_{upper} - V(d_{hkl}))]}{2} \quad \text{(S35)}$$

7.5. Error on averaged quantities

At least four single crystals were measured for each experimental solution concentration value. The standard deviation of their average was calculated as:

$$\sigma_{avg} = \sqrt{\frac{1}{N^2}\left(\sum_{i=1}^{N}\sigma_i^2 + \sum_{i=1}^{N}\sum_{j=i+1}^{N} Cov[x_i,x_j]\right)} \quad \text{(S36)}$$

The standard deviations of individual growth rates were calculated as described in the section above. The errors on the experimental concentration values were calculated by considering the sensitivity of the balance used to measure the mass of solute and solvent used (Mettler Toledo, $1x10^{-4}$g).

8. References

(1) Beckmann, W.; Boistelle, R. Growth Kinetics of the (110) Face of Stearic Acid Growing from Butanone Solutions - Pure Solutions and in the Presence of an Emulsifier. *Journal of Crystal Growth* **1985**, *72* (3), 621–630. https://doi.org/10.1016/0022-0248(85)90213-1.

(2) Beckmann, W.; Kämmer, S.; Meier, J.; Boistelle, R. Growth Kinetics of the (110) Face of the B and C Polymorphs of Stearic Acid Growing from Octanone-2 Solutions. *Journal of Crystal Growth* **1986**, *74* (2), 326–330. https://doi.org/10.1016/0022-0248(86)90121-1.

(3) Sudo, S.; Sato, K.; Harano, Y. Growth and Solvent-Mediated Phase Transition of Cimetidine Polymorphic Forms A and B. *JOURNAL OF CHEMICAL ENGINEERING OF JAPAN* **1991**, *24* (5), 628–632. https://doi.org/10.1252/jcej.24.628.

(4) Kitamura, M.; Furukawa, H.; Asaeda, M. Solvent Effect of Ethanol on Crystallization and Growth Process of L-Histidine Polymorphs. *Journal of Crystal Growth* **1994**, *141* (1–2), 193–199. https://doi.org/10.1016/0022-0248(94)90112-0.

(5) Jiang, S.; ter Horst, J. H.; Jansens, P. J. Concomitant Polymorphism of O-Aminobenzoic Acid in Antisolvent Crystallization. *Crystal Growth & Design* **2008**, *8* (1), 37–43. https://doi.org/10.1021/cg070517n.

(6) Black, J. F. B.; Cardew, P. T.; Cruz-Cabeza, A. J.; Davey, R. J.; Gilks, S. E.; Sullivan, R. A. Crystal Nucleation and Growth in a Polymorphic System: Ostwald's Rule, p-Aminobenzoic Acid and Nucleation Transition States. *CrystEngComm* **2018**, *20* (6), 768–776. https://doi.org/10.1039/C7CE01960B.

(7) Zhu, L.; Wang, L.; Sha, Z.; Wang, Y.; Yang, L.; Zhao, X.; Du, W. Interplay between Thermodynamics and Kinetics on Polymorphic Appearance in the Solution Crystallization of an Enantiotropic System, Gestodene. *Crystal Growth & Design* **2017**, *17* (9), 4582–4595. https://doi.org/10.1021/acs.cgd.7b00335.

(8) Soto, R.; Rasmuson, Å. C. Crystal Growth Kinetics of Piracetam Polymorphs in Ethanol and Isopropanol. *Crystal Growth & Design* **2019**, *19* (8), 4273–4286. https://doi.org/10.1021/acs.cgd.8b01733.

(9) Lynch, A.; Soto, R.; Rasmuson, Å. Single Crystal Growth Kinetics of Two Polymorphs of Piracetam. *Crystal Growth & Design* **2021**, *21* (10), 5631–5640. https://doi.org/10.1021/acs.cgd.1c00455.

(10) Upadhyay, P. P.; Mishra, M. K.; Ramamurty, U.; Bond, A. D. Structure–Property Correlations in Piracetam Polytypes. *CrystEngComm* **2021**, *23* (5), 1226–1233. https://doi.org/10.1039/D0CE01694B.

(11) Gao, Z.; Cen, Z.; Lin, J.; Li, Z.; Fang, L.; Gao, Z.; Han, D.; Gong, J. Synergistic Control of Nonlinear Growth Kinetics and Nucleation Kinetics in the Concomitant Crystallization of Aripiprazole as Reflected by the Ostwald Ratio. *Ind. Eng. Chem. Res.* **2022**, *61* (46), 17183–17195. https://doi.org/10.1021/acs.iecr.2c03731.

(12) Donnay, J. D. H.; Harker, D. A New Law of Crystal Morphology Extending the Law of Bravais. *American Mineralogist* **1937**, *22* (5), 446–467.

(13) Kresse, G.; Hafner, J. Ab Initio Molecular Dynamics for Open-Shell Transition Metals. *Phys. Rev. B* **1993**, *48* (17), 13115–13118. https://doi.org/10.1103/PhysRevB.48.13115.

(14) Kresse, G.; Hafner, J. Ab Initio Molecular-Dynamics Simulation of the Liquid-Metal--Amorphous-Semiconductor Transition in Germanium. *Phys. Rev. B* **1994**, *49* (20), 14251–14269. https://doi.org/10.1103/PhysRevB.49.14251.

(15) Kresse, G.; Furthmüller, J. Efficiency of Ab-Initio Total Energy Calculations for Metals and Semiconductors Using a Plane-Wave Basis Set. *Computational Materials Science* **1996**, *6* (1), 15–50. https://doi.org/10.1016/0927-0256(96)00008-0.

(16) Kresse, G.; Furthmüller, J. Efficient Iterative Schemes for Ab Initio Total-Energy Calculations Using a Plane-Wave Basis Set. *Phys. Rev. B* **1996**, *54* (16), 11169–11186. https://doi.org/10.1103/PhysRevB.54.11169.

(17) Perdew, J. P.; Burke, K.; Ernzerhof, M. Generalized Gradient Approximation Made Simple. *Phys. Rev. Lett.* **1996**, *77* (18), 3865–3868. https://doi.org/10.1103/PhysRevLett.77.3865.

(18) Blöchl, P. E. Projector Augmented-Wave Method. *Phys. Rev. B* **1994**, *50* (24), 17953–17979. https://doi.org/10.1103/PhysRevB.50.17953.

(19) Kresse, G.; Joubert, D. From Ultrasoft Pseudopotentials to the Projector Augmented-Wave Method. *Phys. Rev. B* **1999**, *59* (3), 1758–1775. https://doi.org/10.1103/PhysRevB.59.1758.

(20) Groom, C. R.; Bruno, I. J.; Lightfoot, M. P.; Ward, S. C. The Cambridge Structural Database. *Acta Crystallographica Section B* **2016**, *72* (2), 171–179. https://doi.org/10.1107/S2052520616003954.

(21) Tkatchenko, A.; Scheffler, M. Accurate Molecular Van Der Waals Interactions from Ground-State Electron Density and Free-Atom Reference Data. *Phys. Rev. Lett.* **2009**, *102* (7), 073005. https://doi.org/10.1103/PhysRevLett.102.073005.

(22) Tkatchenko, A.; DiStasio, R. A.; Car, R.; Scheffler, M. Accurate and Efficient Method for Many-Body van Der Waals Interactions. *Phys. Rev. Lett.* **2012**, *108* (23), 236402. https://doi.org/10.1103/PhysRevLett.108.236402.

(23) Ambrosetti, A.; Reilly, A. M.; DiStasio, R. A.; Tkatchenko, A. Long-Range Correlation Energy Calculated from Coupled Atomic Response Functions. *J. Chem. Phys.* **2014**, *140* (18), 18A508. https://doi.org/10.1063/1.4865104.

(24) Mathew, K.; Sundararaman, R.; Letchworth-Weaver, K.; Arias, T. A.; Hennig, R. G. Implicit Solvation Model for Density-Functional Study of Nanocrystal Surfaces and Reaction Pathways. *J. Chem. Phys.* **2014**, *140* (8), 084106. https://doi.org/10.1063/1.4865107.

(25) Mathew, K.; Kolluru, V. S. C.; Mula, S.; Steinmann, S. N.; Hennig, R. G. Implicit Self-Consistent Electrolyte Model in Plane-Wave Density-Functional Theory. *J. Chem. Phys.* **2019**, *151* (23), 234101. https://doi.org/10.1063/1.5132354.

(26) Frisch, M. J.; Trucks, G. W.; Schlegel, H. B.; Scuseria, G. E.; Robb, M. A.; Cheeseman, J. R.; Scalmani, G.; Barone, V.; Petersson, G. A.; Nakatsuji, H.; Li, X.; Caricato, M.; Marenich, A. V.; Bloino, J.; Janesko, B. G.; Gomperts, R.; Mennucci, B.; Hratchian, H. P.; Ortiz, J. V.; Izmaylov, A. F.; Sonnenberg, J. L.; Williams-Young, D.; Ding, F.; Lipparini, F.; Egidi, F.; Goings, J.; Peng, B.; Petrone, A.; Henderson, T.; Ranasinghe, D.; Zakrzewski, V. G.; Gao, J.; Rega, N.; Zheng, G.; Liang, W.; Hada, M.; Ehara, M.; Toyota, K.; Fukuda, R.; Hasegawa, J.; Ishida, M.; Nakajima, T.; Honda, Y.; Kitao, O.; Nakai, H.; Vreven, T.; Throssell, K.; Montgomery, J. A., Jr.; Peralta, J. E.; Ogliaro, F.; Bearpark, M. J.; Heyd, J. J.; Brothers, E. N.; Kudin, K. N.; Staroverov, V. N.; Keith, T. A.; Kobayashi, R.; Normand, J.; Raghavachari, K.; Rendell, A. P.; Burant, J. C.; Iyengar, S. S.; Tomasi, J.; Cossi, M.; Millam, J. M.; Klene, M.; Adamo, C.; Cammi, R.; Ochterski, J. W.; Martin, R. L.; Morokuma, K.; Farkas, O.; Foresman, J. B.; Fox, D. J. Gaussian16 Revision C.01, 2016.

(27) Macrae, C. F.; Sovago, I.; Cottrell, S. J.; Galek, P. T. A.; McCabe, P.; Pidcock, E.; Platings, M.; Shields, G. P.; Stevens, J. S.; Towler, M.; Wood, P. A. Mercury 4.0: From Visualization to Analysis, Design and Prediction. *Journal of Applied Crystallography* **2020**, *53* (1), 226–235. https://doi.org/10.1107/S1600576719014092.

(28) Wulff, G. XXV. Zur Frage Der Geschwindigkeit Des Wachsthums Und Der Auflösung Der Krystallflächen. **1901**, *34* (1–6), 449–530. https://doi.org/10.1524/zkri.1901.34.1.449.

(29) Turner, T. D.; Nguyen, T. T. H.; Nicholson, P.; Brown, G.; Hammond, R. B.; Roberts, K. J.; Marziano, I. A Temperature-Controlled Single-Crystal Growth Cell for the *in Situ* Measurement and Analysis of Face-Specific Growth Rates. *J Appl Crystallogr* **2019**, *52* (2), 463–467. https://doi.org/10.1107/S1600576719002048.

(30) Freeman, H.; Shapira, R. Determining the Minimum-Area Encasing Rectangle for an Arbitrary Closed Curve. *Commun. ACM* **1975**, *18* (7), 409–413. https://doi.org/10.1145/360881.360919.

(31) Offiler, C. A.; Cruz-Cabeza, A. J.; Davey, R. J.; Vetter, T. Crystal Growth Cell Incorporating Automated Image Analysis Enabling Measurement of Facet Specific Crystal Growth Rates. *Crystal Growth & Design* **2022**, *22* (5), 2837–2848. https://doi.org/10.1021/acs.cgd.1c01019.

(32) Cardew, P. T. The Growth Shape of Crystals. *Journal of Crystal Growth* **1985**, *73* (2), 385–391. https://doi.org/10.1016/0022-0248(85)90317-3.

(33) Gadewar, S. B.; Hofmann, H. M.; Doherty, M. F. Evolution of Crystal Shape. *Crystal Growth & Design* **2004**, *4* (1), 109–112. https://doi.org/10.1021/cg034057j.

(34) Bourne, J. R.; Davey, R. J. The Role of Solvent-Solute Interactions in Determining Crystal Growth Mechanisms from Solution: I. The Surface Entropy Factor. *Journal of Crystal Growth* **1976**, *36* (2), 278–286. https://doi.org/10.1016/0022-0248(76)90290-6.

(35) Mullin, J. W. *Crystallisation*, 4th ed.; Butterworth Heinemann: Oxford, UK, 2002; Vol. 6.

(36) Garside, J.; Davey, R. *From Molecules to Crystallizers: An Introduction to Crystallization*; Oxford Chemistry Primers; Oxford University Press: United States, 2000.

(37) Burton, W. K.; Cabrera, N.; Frank, F. C. Role of Dislocations in Crystal Growth. *Nature* **1949**, *163* (4141), 398–399. https://doi.org/10.1038/163398a0.

(38) Ohara, M. *Modeling Crystal Growth Rates from Solution*; Prentice-Hall: Englewood Cliffs, N.J, 1973.

(39) Virtanen, P.; Gommers, R.; Oliphant, T. E.; Haberland, M.; Reddy, T.; Cournapeau, D.; Burovski, E.; Peterson, P.; Weckesser, W.; Bright, J.; van der Walt, S. J.; Brett, M.; Wilson, J.; Millman, K. J.; Mayorov, N.; Nelson, A. R. J.; Jones, E.; Kern, R.; Larson, E.; Carey, C. J.; Polat, İ.; Feng, Y.; Moore, E. W.; VanderPlas, J.; Laxalde, D.; Perktold, J.; Cimrman, R.; Henriksen, I.; Quintero, E. A.; Harris, C. R.; Archibald, A. M.; Ribeiro, A. H.; Pedregosa, F.; van Mulbregt, P.; Vijaykumar, A.; Bardelli, A. P.; Rothberg, A.; Hilboll, A.; Kloeckner, A.; Scopatz, A.; Lee, A.; Rokem, A.; Woods, C. N.; Fulton, C.; Masson, C.; Häggström, C.; Fitzgerald, C.; Nicholson, D. A.; Hagen, D. R.; Pasechnik, D. V.; Olivetti, E.; Martin, E.; Wieser, E.; Silva, F.; Lenders, F.; Wilhelm, F.; Young, G.; Price, G. A.; Ingold, G.-L.; Allen, G. E.; Lee, G. R.; Audren, H.; Probst, I.; Dietrich, J. P.; Silterra, J.; Webber, J. T.; Slavič, J.; Nothman, J.; Buchner, J.; Kulick, J.; Schönberger, J. L.; de Miranda Cardoso, J. V.; Reimer, J.; Harrington, J.; Rodríguez, J. L. C.; Nunez-Iglesias, J.; Kuczynski, J.; Tritz, K.; Thoma, M.; Newville, M.; Kümmerer, M.; Bolingbroke, M.; Tartre, M.; Pak, M.; Smith, N. J.; Nowaczyk, N.; Shebanov, N.; Pavlyk, O.; Brodtkorb, P. A.; Lee, P.; McGibbon, R. T.; Feldbauer, R.; Lewis, S.; Tygier, S.; Sievert, S.; Vigna, S.; Peterson, S.; More, S.; Pudlik, T.; Oshima, T.; Pingel, T. J.; Robitaille, T. P.; Spura, T.; Jones, T. R.; Cera, T.; Leslie, T.; Zito, T.; Krauss, T.; Upadhyay, U.; Halchenko, Y. O.; Vázquez-Baeza, Y.; SciPy 1.0 Contributors. SciPy 1.0: Fundamental Algorithms for Scientific Computing in Python. *Nature Methods* **2020**, *17* (3), 261–272. https://doi.org/10.1038/s41592-019-0686-2.

(40) Barber, C. B.; Dobkin, D. P.; Huhdanpaa, H. The Quickhull Algorithm for Convex Hulls. *ACM Trans. Math. Softw.* **1996**, *22* (4), 469–483. https://doi.org/10.1145/235815.235821.

(41) Liu, Y.; Gabriele, B.; Davey, R. J.; Cruz-Cabeza, A. J. Concerning Elusive Crystal Forms: The Case of Paracetamol. *J. Am. Chem. Soc.* **2020**, *142* (14), 6682–6689. https://doi.org/10.1021/jacs.0c00321.

(42) Schlemmer, H.; Katzer, J. ATR Technique for UV/VIS Analytical Measurements. *Z. Anal. Chem.* **1987**, *329* (4), 435–439. https://doi.org/10.1007/BF00480080.

(43) Billot, P.; Couty, M.; Hosek, P. Application of ATR-UV Spectroscopy for Monitoring the Crystallisation of UV Absorbing and Nonabsorbing Molecules. *Org. Process Res. Dev.* **2010**, *14* (3), 511–523. https://doi.org/10.1021/op900281m.

(44) Cornel, J.; Lindenberg, C.; Mazzotti, M. Experimental Characterization and Population Balance Modeling of the Polymorph Transformation of L -Glutamic Acid. *Crystal Growth & Design* **2009**, *9* (1), 243–252. https://doi.org/10.1021/cg800387a.

(45) Qamar, S.; Elsner, M. P.; Angelov, I. A.; Warnecke, G.; Seidel-Morgenstern, A. A Comparative Study of High Resolution Schemes for Solving Population Balances in Crystallization. *Computers & Chemical Engineering* **2006**, *30* (6–7), 1119–1131. https://doi.org/10.1016/j.compchemeng.2006.02.012.

(46) Qamar, S.; Noor, S.; Seidel-Morgenstern, A. An Efficient Numerical Method for Solving a Model Describing Crystallization of Polymorphs. *Ind. Eng. Chem. Res.* **2010**, *49* (10), 4940–4947. https://doi.org/10.1021/ie9018353.

(47) Neoptolemou, P.; Goyal, N.; Cruz-Cabeza, A. J.; Kiss, A. A.; Milne, D. J.; Vetter, T. A Novel Image Analysis Technique for 2D Characterization of Overlapping Needle-like Crystals. *Powder Technology* **2022**, *399*, 116827. https://doi.org/10.1016/j.powtec.2021.09.017.

(48) Edwards, A. L. *An Introduction to Linear Regression and Correlation.*; An introduction to linear regression and correlation.; W. H. Freeman: Oxford, England, 1976; pp xi, 213.